UNIVERSITA' DEGLI STUDI DI MILANO

Facoltà di Scienze e Tecnologie

HYDROGEN PRODUCTION FROM RENEWABLE PRIMARY SOURCES

BY JOSE LASSO FERNANDEZ

DOTTORATO DI RICERCA IN SCIENZE CHIMICHE
CYCLE XXVIII

Supervisor
Prof. Ilenia Rossetti

Academic Year 2015-16

ABSTRACT

One of the most attracting renewable sources for energy production is bioethanol, which can be obtained from biomass. Special attention is here focused on the steam reforming reaction of ethanol (SRE) in which the principal product, hydrogen, is an interesting energy vector to produce power, electricity and heat. However, the process has not yet come to maturity and it should be optimized in order to make it industrially available.

To this aim, we focused our work on catalysts synthesis for SRE, trying to couple high activity and durability. Different catalyst formulations based on Ni as active phase, supported over zeolite-BEA, zirconia, titania and lanthana were synthesized and characterized by N_2 adsorption/desorption, temperature programmed reduction (TPR), X-rays diffraction, transmission electron microscopy and infra-red Fourier transform spectroscopy. The performance of the catalysts was evaluated for SRE by using absolute ethanol and bioethanol 50 and 90 vol%, obtained from second generation biomass and kindly supplied by Mossi&Ghisolfi. An important aim of the work was the intensification of the process from the energetic point of view, decreasing the energy input to the reformer (endothermal reaction) to better integrate this high temperature stage with the hydrogen purification section and the possible use of Proton Exchange Membrane Fuel Cells (PEM-FC).

Table of Contents

List of Figures

CHAPTER 1

INTRODUCTION AND LITERATURE REVIEW

A general look to the energy world scenario could give an idea of how important is to foster the production of energy from non-traditional sources. The increasing demand of energy due to the impressive industrialization in many countries [1], the evident reduction of fossil fuel reserves, the influence of anthropogenic emissions contributing to the climate change, lead to a growing international pressure to the conservation of the environment. Thus, the dependence from fossil fuels, which requires the development of new sources of renewable energy, is nowadays one of the main challenges for scientists.

Solar, wind and hydro energies as renewables sources are limited for their intermitting nature and the necessity to be developed in a specific place and typically intermittent. By contrast, hydrogen is considered as a promising energy vector, alone or coupled to previously cited sources, to guarantee continuity in energy supply (Fig. 1).

Hydrogen is well-known, since it is the most abundant element in the Universe and it is a base industrial chemical. Hydrogen was proposed as energy vector since the 19^{th} century, however, in more recent years it attracted interest for the conversion of energy through sustainable processes [2-5].

Some raw materials for the industrial hydrogen production are coal and natural gas, but, being fossil sources, H_2 production is associated with greenhouse gas emissions.

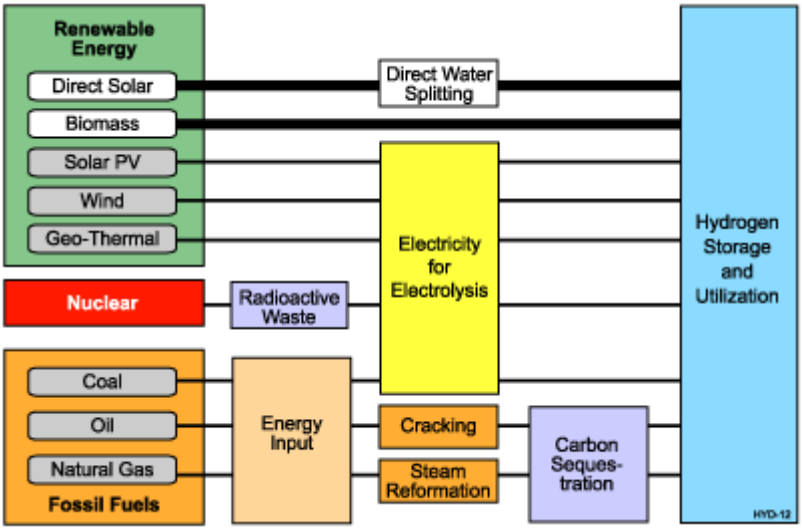

Fig. 1. Hydrogen production paths [6]

The industrial uses of H_2 are huge, e.g. hydrogenation processes in refining, ammonia synthesis [7], methanol synthesis, Fisher-Tropsch process and for the production of inorganic compounds such as HCl, H_2O_2, etc.

In metallurgic industry hydrogen is key element to have non oxidative atmospheres in certain processes or thermal treatments and as reductive agent for the production of iron and other metal such as copper, nickel, uranium, molybdenum, etc. The electronic industry uses hydrogen in the production of doped semiconductors.

Hydrogen is produced in large volumes for industrial processes. The quantities of hydrogen used by the major industries in Western Europe is 19 million tonnes of oil equivalent per year. In energy terms, this is approximately equivalent to 0.5% of the world´s annual oil consumption [8].

In addition, one of the most promising applications for hydrogen is as fuel. In this order can be used directly to produce power through gas turbines or in internal combustion engines, or, with possibly better efficiency, in fuel cells, that could allow to convert its chemical energy content into electrical power with minimal emissions if compared to conventional fuels. However, we already mentioned that it is an energy carrier, not a primary source [9]. Therefore, the overall impact of its combustion/conversion should be carefully accounted for by considering the whole process for its production, purification, transport and use.

In order to improve H_2 foothprint for sustainability reasons, research moved towards renewable sources for its production, considering biomass as raw material (Fig. 2). Biomass can be defined as any organic matter that is available on a renewable or recurring scale, including dedicated energy crops and trees, agricultural residue, algae and aquatic plant, wood and wood wastes, animals wastes, wastes from food and feed processing and other waste usable for the production of energy, fuels and chemicals. Its main feature is relative to the recycle of CO_2, released during transformation of biomass to produce H_2, that can be partially or totally recovered during biomass growth [10,11].

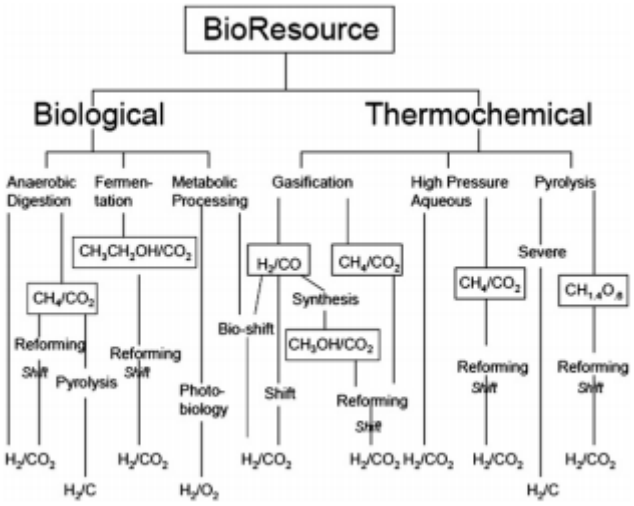

Fig. 2. Pathway from Biomass-to-Hydrogen [12]

That means, the use of biomass-derived raw materials for H_2 production lead to limited CO_2 release or, at best, neutral carbon balance [13, 14-17].

In the field of energy production from biomass, ethanol (called bioethanol) emerged as a promising candidate for hydrogen production because it has high hydrogen content, it is renewable, easy to store, handle and transport and substantially non-toxic [18]. Bioethanol is nowadays very attractive, because it is the most available biofuel worldwide and, as “second generation”, *i.e*. deriving from lignocellulosic biomass, it does not compete with the production of food and feed. Another interesting point is that diluted bioethanol solutions could be used in the case of steam reforming, given the need of steam cofeeding, whereas they are not suitable for combustion. This is a key feature because the anhydrification of bioethanol represents one of its major production costs (50-80% in final product cost). Therefore, the use of diluted bioethanol may be attractive from an economical point of view, provided that it does not contain poisons depressing catalytic activity. This

will be one of the keypoints explored in this thesis, which has been scarcely addressed in the literature.

Steam reforming is a well consolidated refinery process to produce synthesis gas (also called syngas), which is a mixture of H_2, CO and CO_2 that is used directly for the synthesis of methanol or higher alcohols and to produce synthetic fuels through the Fischer-Tropsch synthesis. Alternatively, the reducing capacity of CO can be employed to convert more steam into hydrogen through the water-gas shift reaction.

$$CH_4 + H_2O \rightarrow CO + 3H_2 \qquad \Delta H^o_{298k} = 206.11 \text{ kJ/ mol} \qquad (1)$$

$$CO + H_2O \rightleftharpoons CO_2 + H_2 \qquad \Delta H^o_{298K} = -41 \text{ kJ/ mol} \qquad (2)$$

Steam reforming was developed in Germany at the beginning of the 20th century to produce hydrogen for ammonia synthesis and it was further improved in the 1930s when natural gas and other hydrocarbon feedstocks such as naphtha became available on a large scale. The active metal area is relatively low, of the order of only a few $m^2\ g^{-1}$. The process is industrially operated at high temperatures (up to 1000°C) and moderate pressures (25-35 bar).

Traditionally, the steam reforming reactor has a tubular design with vertical tubes, loaded with the catalyst. They are surrounded by furnaces to supply the heat required for the strongly endothermic process, see Fig. 3. Combustion of natural gas supplies the heat to the tubes.

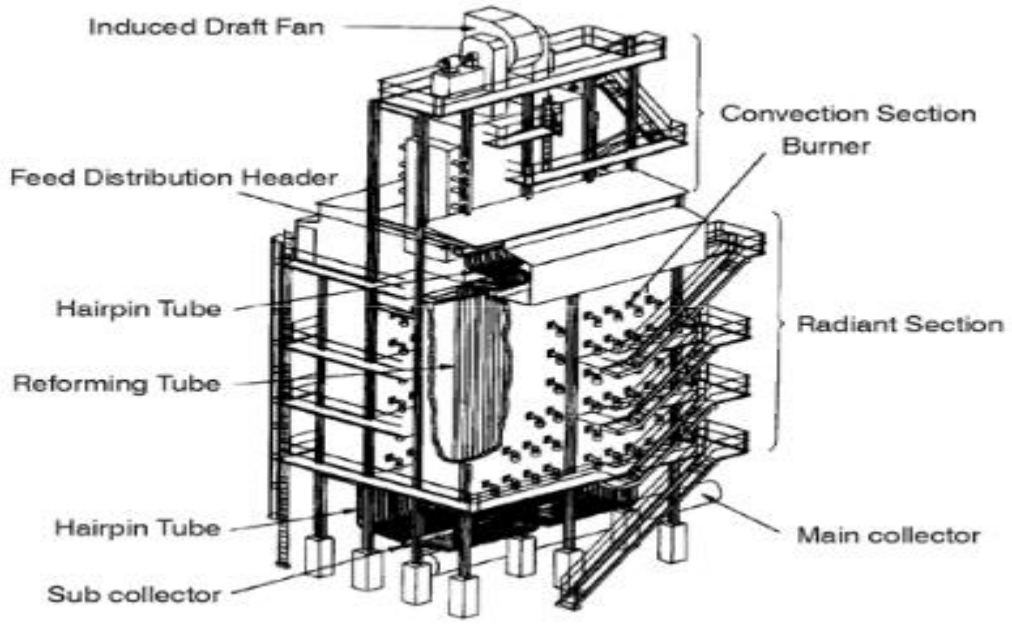

Fig. 3. Topsoe reformer with burners placed on side walls. [19]

In steam reforming the catalysts and operating conditions are searched to favor the water gas shift reaction (WGS), which converts CO to CO_2 with further H_2 production [20]. However, there is a mismatch between the high temperature required by SR (endothermal) and the low temperatures which thermodynamically favour WGS (moderately exothermal). Thus the optimization of reaction temperature, which will be one of the goals of this thesis, is important to improve H_2 yield.

As recalled above, in order to improve the sustainability of H_2 production, the steam reforming process has been adapted to different biomass-derived compounds, among which ethanol has many interesting features and seem an ideal candidate. Steam reforming of ethanol (SRE) is an endothermal process

which takes place according to the following stoichiometric reaction, Eq. (3):

$$CH_3CH_2OH + 3H_2O \rightarrow 6H_2 + 2CO_2 \qquad (\Delta H^o_{298} = +347.4 \text{ kJ mol}^{-1}) \qquad (3)$$

Including the water-gas shift of the intermediate CO (Eq. (2)), which further increases the hydrogen yield with respect to syngas production [18]:

$$CO + H_2O \rightleftharpoons CO_2 + H_2 \qquad (\Delta H^o_{208} = +41 \text{ KJ mol}^{-1}) \qquad (4)$$

Nevertheless, the overall process is a complex network of reactions, such as ethanol dehydrogenation, dehydration or decomposition, which can lead to the formation of several byproducts (acetaldehyde, ethylene and methane respectively) [21,22] (Fig 4). Furthermore, at high temperature one challenge for SR is catalyst deactivation by sintering, so that high thermal resistance is a pressing need. By contrast, it is envisaged to operate SR at lower temperature, to lower the heat input to the reactor (process intensification). Unfortunately the formation of coke easily occurs at temperature lower than 600°C.

The formation of coke, recently reviewed by Mattos et al. [7], is believed to occur through the Boudouard reaction ($2CO \leftrightarrow CO_2 + C$), the decomposition of methane ($CH_4 \leftrightarrow C + 2H_2$) or the polymerization of ethylene [23], which is formed by ethanol dehydration. Coke deposition can be controlled by properly tuning the operating

conditions (*i.e.* steam-to-ethanol ratio, reaction temperature) [24], but the formulation of the catalyst plays a key role as well [23].

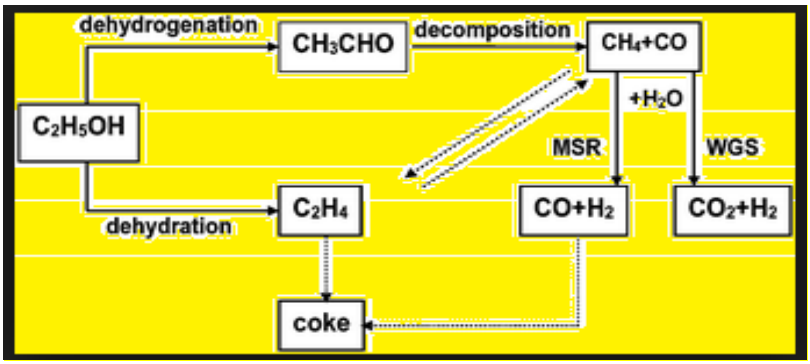

Fig.4. Possible SRE reaction pathways [5].

Coking is particularly significant around 500°C, because coke forms, but it is not effectively gasified by steam, so it can accumulate over catalyst surface. Nevertheless, it would be very advantageous being able to operate around this temperature, because some catalyst formulations demonstrated satisfactory activity and selectivity and this relatively low temperature. This would limit the energy input to the process with respect to common reaction conditions with fossil hydrocarbons (T > 750°C). Therefore, improving catalyst resistance to coking represents a milestone for the development of low temperature SRE [18].

If suitable active phases are reported in the literature to achieve satisfactory hydrogen yield from ethanol, catalyst resistance to deactivation by sintering, coking and poisoning remains a less explored field, which has nevertheless a huge importance from the applicative (industrial) point of view.

Different metal active phases have been proposed for the steam reforming of ethanol. The late transition metals such as Pd, Pt, Ru, Rh and Ir can be effectively

used as very active catalysts for steam reforming, but Ni-based catalysts are economically the most feasible. Ru, Rh and other noble metals are more active than Ni, but are less attractive due to their cost [19], whereas Fe and Co are in principle active, but they easily oxidize under the process conditions. Ni, Co and Cu are active for this application as the less expensive non-noble metals.

Among the studies carried out on metal active phase for steam reforming of ethanol, the most interesting results have been obtained with Co and Ni, being the latter the most promising one. [13, 14, 25-29].

Verykios et al-has studied H_2 production by SRE at first focusing on Ni as active phase loaded on different supports [30, 31] and on supported noble metals [32]. Other papers on SRE have reported that it is possible to reduce the coke formation and lower the reduction temperature [33-35].

Ni is a highly active and selective active phase for SRE because of its high capability to break C-C bonds and also to promote the water-gas shift reaction, thus increasing hydrogen yield [25, 36]. It is cheaper and more available than noble metals, although it may be quickly deactivated by coking and sintering [37]. However, with Ni as active phase, there is a better control of dispersion, *e.g*. through strong metal support interaction, that allows to reduce the particles size and thus the coke formation. In particular, coking is thought to occur more promptly over large Ni particles and aggregates [38-40] than over much dispersed crystallites. Indeed, carbon filaments can be formed if carbide intermediates accumulate at the interface between the metal particle and the support surface. Therefore, small Ni particles are less prone to filaments formation because the

interface saturates quickly. Furthermore, strong acidity may lead to ethanol dehydration to ethylene, which oligomerises and polymerises. The dehydration activity is competitive with the dehydrogenation/decomposition route, which leads to acetate/glycolate surface intermediates, readily decomposed into products ($CO/CO_2/H_2$) or reformable intermediates such as methane and acetaldehyde.

Therefore, suitable strategies to limit coke accumulation are the effective control of acidity [41-43] (typically by adding a basic promoter) and the improvement of metal dispersion. This is particularly challenging due to the high operating temperature of the process, so that high dispersion should be guaranteed also during operation. The latter features may be improved by strenghtening the metal-support interaction: the strongest the latter, the highest the metal dispersion (and its stability towards sintering) [44, 45, 46].

As a result, the nature of the support contributes to the activity and stability of the catalyst. It should possess a good chemical and mechanical resistance and a high surface area, in order to favor the dispersion of the active phase [47, 48].

In the literature, the most used support is alumina, for direct transposition from the industrial catalysts for the SR of methane. Acidity is not a fundamental issue for that application, whereas ethanol dehydration is a path towards coking and it is favored by strong support acidity. Therefore, for SRE alumina is usually doped with alkali or lanthana to limit its acidity [22, 29, 49-51].

Although aluminium oxide exits in various structures, only three phases are of interest, namely the nonporous, crystallographically ordered α-Al_2O_3 and the

porous amorphous *η*- and *γ*-Al_2O_3. As a support, *γ*-Al_2O_3 offers high surface area (50-300 m^2g^{-1}), mesopores between 5 and 15 nm, pore volume *ca*. 0.6 $cm^3\ g^{-1}$, high thermal stability and the ability to be shaped into mechanically stable extrudates and pellets. Its surface contains hydroxyls, between 10 and 15 OH per nm^2, the linear ones being Brønsted acids (H^+ donor). After dehydration, the surface develops Lewis acidity (electron acceptor) on the uncoordinated Al sites. The highly stable α-Al_2O_3 is used in high temperature applications, such as in steam reforming at extremely high temperature, or in cases where low surface are desired [19], but its very low surface area is a major drawback.

The acidity of alumina can be a minor problem for high temperature operation. By contrast, during operation at low temperature SiO_2 can be used as support. Silica

with surface area up to 300-500 $m^2\ g^{-1}$ can be prepared by different techniques. Though silica supports are amorphous, the surface may exhibit some local order such as that of the mineral *β*-crystoballite. The surface of silica contains OH groups at densities of between 4 and 5.5 OH per nm^2; that of cristobalite is 4.55 OH per nm^2. Silica surfaces contain only terminal OH groups, *i.e*. bound to a single Si atom [19].

Recent results of our research group highlighted, on one hand, the importance of the stability of the support in the reaction conditions, on the other hand the key role of the metal-support interaction in determining both activity and stability of the catalyst with time on stream [44, 45, 52]. In particular, a strong interaction stabilizes the active phase, preserving it from sintering and, thus, from coking phenomena [18].

In addition, the catalyst preparation procedure determines the success of a formulation.

The principal traditional ways to prepare catalysts are:

1) By coprecipitating the catalytically active component and the support to give a mixture that is subsequently dried, calcined (heated in air) and finally reduced to yield a porous material with a high surface area;
2) By loading pre-existing support materials in the form of shaped bodies with the catalytically active phase by means of impregnation or precipitation from a solution. This is the preferred method when catalyst precursors are expensive and the aim is to deposit the catalytically active phase in the form of nanometer-sized particles on the support. All noble metal-based catalysts are manufactured in this way [19].

A new versatile technique is Flame Spray Pyrolysis (FP), a high temperature synthesis procedure characterized by high productivity. Provided that a solvent with sufficiently high combustion enthalpy is chosen, FP is able to impart high thermal stability in addition to tune metal dispersion. Indeed, the FP technique allows the continuous and one-step synthesis of oxides, single or mixed, usually showing good phase purity, along with nanometer-size particles and, hence, veryhigh surface area (up to 250 m^2/g). The later parameter could help improving the performance at low temperature, whereas thermal stability is a must during high temperature application [41, 52-54]. Therefore, this synthesis has been used

here to cope with some of the criticisms as for catalyst resistance to deactivation and coking, as above discussed.

Our home-made FP apparatus is composed of three sections (Fig. 5):

a) The flame reactor (burner)
b) The feeding rate control devices for supplying gaseous and liquid reagents
c) The catalyst powder collection system

The burner consists of a capillary tube (inner diameter = 0.6mm) ending in the centre of a vertical nozzle and connected with a syringe pump (Harvard, mod. 975), feeding the solution of the mixed oxide precursors. The nozzle is fed with oxygen (99.95%), acting both as oxidant and as dispersing agent, able to form micro-droplets of solution. The main flame is ignited and supported by a ring of

twelve premixed O_2 + CH_4 flamelets. Gas flow rate is regulated by MKS (mod. 1259 C) mass flow meters, controlled by a MKS (mod. 247 C) control unit.

The synthesized nano-particles are collected by means of a 10 kV electrostatic precipitator [55]. Since the preparation method determines the physico-chemical properties of the catalysts, in previous work [56] we carried out studies on silica and zirconia nickel supported catalysts for use in the steam reforming of ethanol considering the productivity and stability towards coking and sintering. In this order

the catalysts were prepared by precipitation for support synthesis and subsequent impregnation with the active phase and by flame pyrolysis synthesis. As result we observed that preparation different methods clearly attributed to the

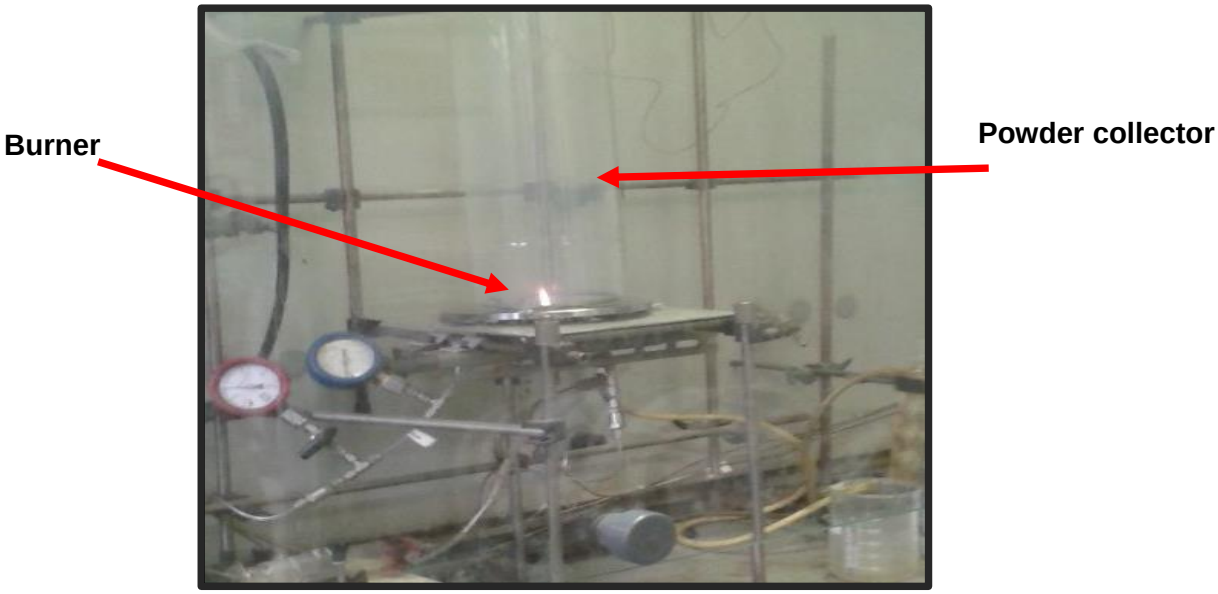

Fig. 5. Flame Pyrolysis apparatus

samples different textural, structural and morphological properties, as well as different reducibility and thermal resistance.

In addition, in previous work we also focused on catalyst stability by using as active phase Ni, Co and Cu supported over Silica and Zirconia at reaction temperature of 300-500°C. It should be mentioned that the selection of the respective supports was based on their different acidity and redox properties with respect to the most commonly used alumina [56].

Ni supported over zirconia and prepared by flame pyrolysis exhibited much smaller metal particles size ca. 2.5 nm (but also smaller particles for the support) than Ni catalyst over silica. While Cu over silica resulted to have big particles and less defined cobalt oxides for Co-silica sample. Moreover, higher metal dispersion was obtained with Ni-zirconia catalyst than with Ni supported over silica. As well known,

strongest metal-support interaction its ascribed to well dispersed active phase over the surface of the support [57 - 59].

These results confirm that catalyst method preparation is key factor to impart the desired features for the catalyst and flame pyrolysis demonstrated to be more effective than traditional impregnation and co-precipitation methods.

Another important base for this work it constituted by the study carried out on Ni, Co and Cu supported over TiO_2 by preparing the samples following different procedures, tuning the reducibility of the active phase and its interaction with the support. TiO_2 support was selected considering its different acidic and redox properties with respect to other supports, such as silica or zirconia. [57 - 59]. In this work, Ni confirmed the most active metal for SRE, within those investigated, but remained a significant coking activity, in which Ni played an important role with lower contribution of support acidity.

AIM OF THE THESIS

Considering the exposed literature and the principal objective of production of sustainable energy from renewable sources, the aim of this work was to optimize the SRE process, possibly at the lowest temperature, through the development of different Ni-based catalysts characterized by high catalytic activity and limited coke formation. The resistance to deactivation was improved thanks to a good thermal stability and high active phase dispersion. The overall work was carried out through the following scheme:

1) Effect of active metal loading and dispersion. We focused on two catalytic systems:

A) Ni over Zeolite with different initial Si/Al ratio and further dealumination.

The approach was to improve metal dispersion in a high surface area matrix such as zeolite in whose microporous channels, the Ni metal active phase was entrapped to prevent its sintering. In this order were considered the effect of Ni loading and support acidity by preparing different zeolites with different initial Si/Al ratio and further dealumination, in order to assess also the effect of support acidity.

B) Ni-based catalysts supported over Titania and Lanthana prepared by FP.

To impart suitable thermal resistance and provide high metal dispersion to the catalyst, we selected FP as a high temperature synthesis, which was systematically compared with liquid phase preparation of the supports (e.g. by precipitation), followed by impregnation of the active phase. The catalysts were

supported over TiO_2 and La_2O_3, also in this case to address the effect of different acidity.

2) Effect of bioethanol concentration and purity. To evaluate the effect of bioethanol concentration on the activity of our selected Ni based catalysts, supported over zirconia, we tested different samples of second generation bioethanol 90 and 50 vol% in comparison with absolute ethanol.

3) Control of coke formation by adding basic oxides species. The control of support acidity on Ni-based catalysts supported over ZrO_2 was done by doping with Ca, oxide. Also the preparation method of the catalysts was considered, comparing traditional preparation procedures with FP.

CHAPTER 2

EXPERIMENTAL: CATALYSTS PREPARATION AND CHARACTERIZATION

1. Ni-BEA catalysts

1.1. Preparation and characterization

Nine different samples of Ni/BEA catalysts have been prepared starting from commercial zeolite supports, characterized by different acidity (Al content) and Ni loading.

Tetraethylammonium BEA (TEABEA) zeolites with Si/Al ratio of 12.5 and 17 (mol/mol) provided by RIPP (China) were calcined in air (100°C/h) at 550°C for 15 h under static conditions to remove the organic template. Both the organic-free BEA zeolites were treated two times with 400 ml of 0.1 mol/L NH_4NO_3 solution during 3 h in order to exchange K^+ and Na^+ ions present in industrial BEA zeolite with NH_4^+ ion. Then the solids were washed with distilled water and dried overnight at 90°C. The NH_4AlBEA samples were calcined in air (100°C/h) for 3 h at 500°C under static conditions to remove NH_3 and obtain the acidic form of the zeolite HALBEA (I) and HALBEA (II), with Si/Al ratio of 12.5 and 17 (mol/mol) respectively.

The treatment of the zeolites with Si/Al ratio 12.5 and 17 (mol/mol) with nitric acid (13 mol/L) at 80°C under stirring in air lead to removing of the organic template (TEA) and Al atoms. The treatment has been carried out for short (0.08 h, partial

deallumination) or prolonged time (4h, deep deallumination). Ni was added by wet impregnation from a $Ni(NO_3)_2$ $6H_2O$ solution. Proper amount of Ni precursor was dissolved in 200 mL water and the solid suspension was stirred for 24 h at r.t. at pH of 3.3. Then, the suspension was stirred in evaporator under vacuum of a water pump for 2 h in air at 60°C until the water was completely evaporated.

X-ray powder diffraction (XRD) analysis was carried out at room temperature by means of a PHILIPS PW1830 diffractometer with Bragg-Brentano θ - 2θ geometry. The Cu Kα radiation (λ = 1.5406 Å) was used. Intensities were collected over a 21° – 90° 2θ range with 0.03° step size and 4s step time. The apparatus was provided with graphite monochromator. The voltage and current intensity of the generator were set at 40 kV and 30 mA respectively. The Rietveld method [60] was used for the XRPD data refinement using TOPAS software [61].

Specific surface area and pores size distribution were evaluated trough N_2 adsorption-desorption isotherms at -196^{o}C (Micromeritics, ASAP 2020). Surface area was calculated on the basis of the BET equation, whereas the pores size distribution was determined by the BJH method, applied to the N_2 desorption branch of the isotherm. Micropores volume and area were determined from the t-plot analysis. Prior to the analysis the sample was outgassed at 300°C overnight. The temperature Programmed Reduction (TPR) technique was employed to identify different metallic species possibly present in the catalysts according to the different reduction temperatures, in case used to assess the interaction strength between the active phase and the support. The catalyst was placed in a quartz

reactor and heated by 10°C/min from r.t. to 800°C in a 5% H_2/Ar mixed gas stream flowing at 40 mL/min.

Temperature Programmed Oxidation (TPO) was carried out on the reduced sample by feeding 40 mL/min of 10 vol% O_2/He gas mixture while heating by 10°C/min from r.t. to 800°C.

SEM images have been obtained using a Field Emission Gun Electron Scanning Microscopy LEO 1525, after metallization with Cr. Elemental composition was determined using a Bruker Quantax EDS.

TEM images have been obtained using a Phillips 208 Transmission Electron Microscope. The samples were prepared by putting one drop of an ethanol dispersion of the catalysts on a copper grid pre-coated with a Formvar film and dried in air.

FT-IR spectra have been recorded in static conditions by a Nicolet Nexus Fourier transform instrument, using conventional IR cells connected to a gas manipulation apparatus. Pressed disks of pure catalyst and support powders (~30 mg) were activated by prolonged outgassing at 500°C. Pyridine (py, Aldrich, pur. 98%) adsorption experiments have been performed over the activated samples at r.t. and following outgassing at increasing temperature.

1.2 Activity testing

Activity tests were carried out in a micropilot plant in which a downflow reactor (Incoloy 800) with 0.9 cm of internal diameter and 40 cm length was placed and heated by an electric oven connected to a Eurotherm 3204 (Fig. 6).

The catalysts (*ca*. 0.5 g, 0.15-0.25 mm particle size) were diluted 1:3 (vol/vol) with SiC of the same size. The void space of the reactor was filled with quartz beads, *ca*. 1mm in size. The catalyst was activated in 50 cm^3/min of 20% H_2/N_2 gas mixture, while heating by 10 °C/min up to 800°C for 1h when testing was carried out at 500-625-750°C and other samples at 500°C for testing at low temperature, *i.e*. 500-400-300°C**.**

Activity testing was carried out by feeding 0.017 cm^3/min of 3:1 (mol/mol) H_2O:CH_3CH_2OH liquid mixture by means of a Hitachi, mod L7100, HPLC pump, added with 56 cm^3/min of N_2, used as internal standard, and 174 cm^3/min of He. Such dilution of the feed stream was calibrated so to keep the reactants mixture in the vapor phase even at zero conversion at the reactor outlet.

Fig. 6 Micro pilot plant for SRE

The 3:1 (mol/mol) water/ethanol ratio corresponds to *ca.* 50 vol% solutions, which are easily obtainable from the bioethanol fermentation broth through a flash drum.

This allows to use a much less expensive feedstock than heavily dehydrated ethanol, considering that bioethanol purification costs impact for 50-80% on its production costs [62] .

The activity tests were carried out at atmospheric pressure, GHSV = 2500 h^{-1} (referred to the ethanol + water gaseous mixture) 750°C, 625°C and 500°C for some interesting samples.

The analysis of the out-flowing gas was carried out by a gas chromatograph (Agilent, mod. 7980) equipped with two columns connected in series (MS and Poraplot Q) with a thermal conductivity detector (TCD), properly calibrated for the detection of ethanol, acetaldehyde, acetic acid, acetone, water, ethylene, CO, CO_2, H_2. Material balance on C-containing products was checked to quantify coke deposition. Repeated analysis of the effluent gas were carried out every hour and the whole duration of every test was ca. 8 h.

The raw data, expressed as mol/min of each species outflowing from the reactor, averaged over 4-8 h-on-stream, have been elaborated [44] as follows to calculate:

Products distribution [28]: Yi = mol *i* / (mol *i*)

C balance: 100 – (((mol CH_3 CH_2 OH * 2)$_{in}$ – Σ(molC_i *X_i)$_{out}$)/(mol CH_3 CH_2 OH * 2)$_{in}$)*100 (as a measure of coking)**Conversion**: X_i = (mol i_{in} – mol i_{out})/mol i_{in} i = H_2O, CH_3 CH_2 OH

Selectivity: S_i = (mol i /v_i) (mol ethanol $_{in}$ – mol ethanol$_{out}$)

H_2 yield: Yield = $X_{ethanol}$ * SH_2 = mol H_2 / vH_2 * mol ethanol$_{in}$

H_2 productivity: mol H_2 out/min Kg_{cat} where i= products detected, dry basis;

X_i = number of C atoms in the ith molecule; v_i = stoichiometric coefficient of species i in the ESR reaction.

2. Ni/La_2O_3 and Ni/TiO_2 catalysts

2.1 Preparation and characterization

The FP methods was chosen because it produces metal oxides with features suitable for SR, such as high thermal stability coupled with high surface area [55, 62-64]. A first set of samples was directly prepared by FP, inserting in one step the Ni active phase, in the form of oxide precursor, into the selected support with different metal loading. For comparison, the same formulations have been prepared by impregnation of Ni on the FP prepared supports. Two supports were also compared, *i.e.* TiO_2 and La_2O_3, characterized by different surface acidity and redox properties.

TiO_2 was prepared from titanium isopropoxide (Aldrich, purity 97%) dissolved in o-xylene (Aldrich, purity 97%) with a 0.1 mol/L final concentration referred to TiO_2.

La_2O_3 was produced from lanthanum acetate (Aldrich, purity 99.9%), dissolved in propionic acid (Aldrich, purity 97%) and diluted with o-xylene (1:1 vol/vol) achieving a final concentration of 0.1 mol/L referred to La_2O_3.

The solutions were feed to the home-designed burner [44] with 2.2 mL/min flow rate and 1.5 bar pressure drop across the nozzle. The latter was co-feed with 5 L/min of O_2.

In case of catalysts prepared in one-step by FP the active metal was directly incorporated during the support synthesis. Ni was added to the above mentioned mother solutions by dissolving Ni acetate (Aldrich, purity 98%) in propionic acid. Nominal Ni loading was 5, 10 and 15 wt% on both supports. A perovskitic catalyst precursor ($LaNiO_3$) was also prepared, for which the mother solution was prepared with a La/Ni ratio = 1 (mol/mol). The same catalyst formulations were prepared from the FP-synthesized TiO_2 and La_2O_3 by adding Ni by wet impregnation with an aqueous solution of $Ni(NO_3)_2$.

The catalysts were reduced post synthesis for 1 h at 800°C in a 20 vol% H_2 /N_2 gas mixture.

Samples codes are denoted as x-Ni/y-z, where “x” represents Ni wt%, “y” is “T” for TiO_2 and “La” for La_2O_3 supports respectively, z = “F” or “I” for samples prepared in one step by FP or added by impregnation on the FP-prepared support.

X-rays diffraction (XRD) analysis was performed on a Phillips PW3020 instrument.

Specific surface area and pore size distribution were evaluated through the collection of N_2 adsorption-desorption isotherms at 77K on a Micromeritics ASAP 2010 instrument. Surface area was calculated on the basis of the Brunauer, Emmet and Teller equation (BET), whereas the pores size distribution was determined by the BJH method, applied to the N_2 desorption branch of the isotherm. Prior to the analysis the samples were outgassed at 300^{o}C overnight.

Scanning electron microscopy (SEM) has been carried out using a Phillips XL-30CP instrument and the surface and elemental composition of the catalysts was determined using energy dispersive X-ray analysis (EDX). The scanning electron microscope was equipped with a LabB6 source and an EDAX/DX4 detector. The acceleration potential voltage was maintained between 15 keV and 20 keV and samples were metallized with gold.

Transmission electron microscopy (TEM) was performed with a Phillips XL-30CP electron microscope.

Temperature programmed reduction (TPR) was performed by placing the catalyst in a quartz reactor and heating at 10°C/min from 25 to 800°C in a 5 vol% H_2 /Ar stream flowing at 40 mL/min. H_2 consumption was monitored continuously by means of a mass spectrometer (MS).

2.2 Activity testing

Activity tests were performed by means of the system described in part 1.2.

3. Ni/ZrO_2 catalysts

3.1 Preparation and characterization

Code for Ni/ZrO_2 prepared catalysts by impregnation (I) and prepared by flame pyrolysis (F):

10wt% Ni/ZrO_2 = ZNi-I

10wt% Ni/ZrO_2 with CaO (9 wt%) = ZCaNi-I

$Zr(OH)_4$ was prepared by a precipitation method [36] at a constant pH of 10.

$ZrOCl_2*8H_2O$ (Sigma-Aldrich, purity ≥99.5 %) was dissolved in distilled water and added with a peristaltic pumper under vigorous stirring to an ammonia (33 %, Riedel-de Haën) solution. During the precipitation, the pH value was kept constant at 10.0 ± 0.1 by the continuous addition of 33% ammonia solution.

After the complete addition of the salt solution, the hydroxide suspension was aged for 20 h at 90°C, then filtered and washed with warm distilled water until it was free from chloride ions ($AgNO_3$ test). The samples were dried overnight at 110°C.

$Zr(OH)_4$ was impregnated with an aqueous solution containing both, the metal [$Ni(NO_3)_2*6H_2O$, Sigma-Aldrich, purity ≥98.5%] and the dopant [$Ca(NO_3)_2*4H_2O$, Fluka, purity ≥ 99%] precursors.

The active phase (Ni) and the dopant (CaO) were added to both $Zr(OH)_4$ preparations simultaneously by means of the incipient wetness impregnation technique. Ni was kept constant in all the samples (10 wt%), whereas CaO varied (0, 3, 6, 9 wt%). All the samples are reported in the following chapter (3.7). They were dried overnight at 110°C and finally heated (2°C/min) up to 500°C in flowing air (30 mL/min STP) and kept at this temperature for 4 h. The reference sample, Ni/ZrO_2, is labelled as *ZCa_xNi*, where Ca_x denotes the CaO amount as wt%.

A different set of samples was prepared by FP and labelled with the following code:

10wt% Ni/ZrO_2 = ZNi-F

10wt% Ni/ZrO with CaO (9wt%) = ZCaNi-F

The precursor of zirconia, zirconium acetyl-acetonate $Zr(C_5H_7O_2)_4$ Aldrich+99%) and the base oxide precursor $Ca(CH_3COO)_2$ (Aldrich ≥ 99%) are dissolved in propionic acid. After the complete solubilisation, the solution was transparent and nickel acetate, Ni(II) $(CH_3CO_2)_2 \cdot 4H_2O$ (Aldrich 98%) was added, also being dissolved. Before injection of the prepared solution to the burner, the solution is diluted 1:1 (vol/vol) with o-xylene (Aldrich pur. 97%) to increase flame temperature.

Specific surface area and pores size distribution were evaluated through N_2 adsorption-desorption isotherms at – 196°C (MICROMERITICS, ASAP 2000 Analyser). Surface area was calculated on the basis of the BET equation [64], whereas the pores size distribution was determined by the BET method, applied to the N_2 desorption branch of the isotherm [65]. Prior to the analyses the samples

were reduced in H_2 flow for 1 h at 500°C, dried overnight at 110°C and then outgassed in vacuum at 300°C for 2 h.

X-ray powder diffraction (XRD) patterns were measured by a Bruker D8 Advance diffractometer equipped with a Si(Li) solid state detector (SOL-X) and a sealed tube providing Cu Kα radiation. The Rietveld refinement method as implemented in the Bruker TOPAS programme was used to obtain the refined unit cell parameters, crystal size and the quantitative phase analysis for the ZrO_2 support and metal phases in the samples. The crystal size determination was achieved by the integral breadth based calculation of volume weighted mean crystallize sizes assuming intermediate crystallite size broadening modelled by a Voigt function. The samples were reduced in H_2 flow for 1 h at 500°C before the analysis.

Temperature programmed reduction (TPR) measurements were carried out by placing the catalyst in a quartz reactor and heating in a 5% H_2/Ar mixed gas stream flowing at 40 mL/min at a heating rate of 10°C/min from 25 to 700°C. H_2 consumption was monitored by a TCD detector.

Temperature programmed oxidation (TPO) of the spent catalysts was carried out by feeding 40 mL/min of a 10°C/min from 25 to 650°C.

O_2 pulse chemisorption measurements were performed at 25°C by means of a lab-made equipment. Before chemisorption the sample (100 mg) was reduced in H_2 flow (40 mL/min) at 500°C for 1 h and then evacuated under helium gas at 500°C for 2 h to remove all physisorbed hydrogen). A Ni/O_2 chemisorption stoichiometry = 2 was used [64].

In situ FTIR spectra were obtained on a Perkin Elmer 2000 spectrophotometer (4 cm^{-1} resolution, MCT detector). Reduced samples were inspected in the form of self-supporting tables (~25 mg cm^{-2}). Quartz cells (equipped with KBr windows) connected to a gas vacuum line equipped with rotary and turbo-molecular pumps (residual pressure $p < 10^{-5}$ Torr) were used. The samples were activated in oxygen at 300°C. FTIR spectra of probe molecules (CO) adsorbed thereon were also run, in order to obtain information on surface acidity.

High-Resolution Transmission electron microscopy (HR-TEM) images were obtained by using a JEOL JEM 3010UHR (300 kV) TEM fitted with a single crystal LAB_6 filament and an Oxford INCA Energy TEM 200 energy dispersive X-ray (EDX) detector. All samples were dry deposited, after their reduction, on Cu “holey” carbon grids (200 mesh).

SEM images have been obtained using a Field Emission Gun Electron Scanning Microscopy LEO 1525, after metallization with Cr. Elemental composition was determined using Bruker Quantax EDS.

HR-TEM images of spent samples have been obtained using a Philips 208 Transmission Electron Microscope. The samples were prepared by putting one drop of an ethanol dispersion of the catalysts on a copper grid-coated with a Formvar film and dried in air.

Micro–Raman sampling was made by an OLYMPUS microscope (model BX40) connected to an ISA Jobin-Yvon model TRIAX320 single monochromator, with a resolution of 1 cm^{-1}. The source of excitation was a Melles Griot 25LHP925 He-Ne

laser that was used in single line excitation mode at l =632.8 nm. The powder focused on the samples was always less than 2mW. The scattered Raman photons were detected by a liquid-nitrogen cooled charge coupled device (CCD, Jobin Yvon mod.Spectrum One).

3.2 Activity testing

Activity tests were performed by means of the system described on part 1.2. The catalysts were activated in a 50 cm^3 /min of a 20 vol% H_2 /N_2 gas mixture while heating by 10^{o}C /min up to 500°C. The activity tests were carried out at atmospheric pressure, GHSV =2500 h^{-1} (referred to the ethanol + water gaseous mixture) at 500°C. Additional activity tests at 400 and 300°C as well as a long term run (*ca.* 100 h-on stream) were also carried out on the most promising sample by using pure ethanol and bioethanol 90 vol% and 50 vol%. Some samples were also tested at GHSV = 7755 h^{-1} to better highlight their catalytic performance.

CHAPTER 3

RESULTS AND DISCUSSION

3.1 Characterization of Ni-BEA catalysts

BEA zeolite is an special class of oxides, but also due to its channels and cages in which cations, water and adsorbed molecules may reside and react (Fig. 7). The BEA microporous structure is constituted by channels *ca.* 6.7 Å in size, allowing the diffusion of ethanol with limited resistance [64], since almost all the accessible free volume of the pores is available given the characteristic molecular size of ethanol (*ca.* 3.8 Å) [65]. For fundamental catalysis they offer the advantage that the crystal structure is known and the catalytically active sites are well defined. Its structure basically consist of SiO_4 and AlO_4 tetrahedra (Fig. 8) , which can be arranged by sharing O-corner atoms in many different ways to built a crystalline lattice. The SiO_4 tetrahedra can be arranged into several silicate units, e.g. squares, six or eight-membered rings, called secondary building blocks. Zeolite structures are built up by joining a selection of building blocks into periodic structures [68].

In its pore system, when Al^{3+} replaces Si^{4+} ions atoms in the tetrahedral, the units have a net charge of -1, and hence cations such as Na^+ or, most important H^+, are needed to neutralize the negative charge. The number of cations present within a zeolite structure equals the number of alumina tetrahedral in the framework.

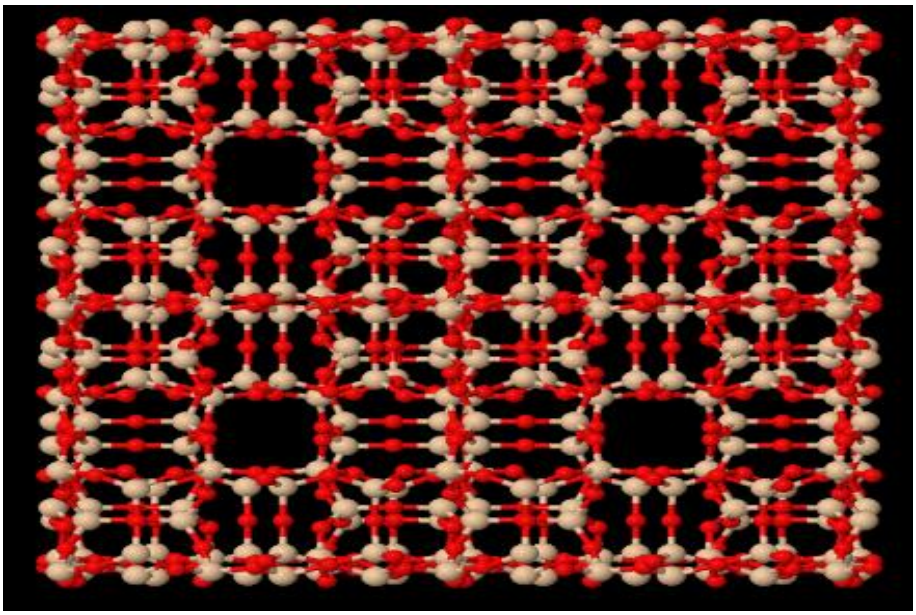

Fig. 7. Silicate units of BEA zeolite [69]

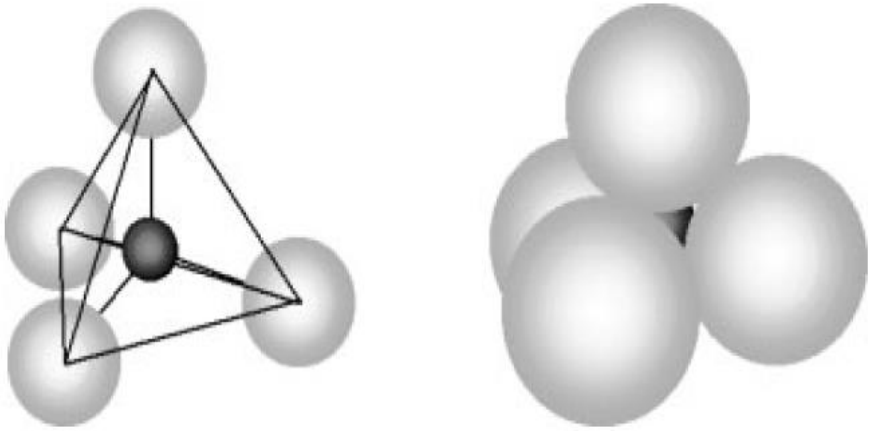

Fig. 8. SiO_4 tetrahedra from the basic building blocks of zeolite [19]

Textural, structural and morphologic properties of NiBEA catalysts

The following table shows the list of samples used.

Table 1: Nomenclature, preparation parameter and main physical-chemical properties of the samples prepared. SSA= Specific Surface Area, reported as BET and micropore area from- t-plot (the latter between parentheses).

Sample	Code	Initial Si/Al (atom/atom)	Post-treatment	Ni content (wt%)	Si/Al (mol/mol) EDX	SSA (m^2/g)
1	$Ni_{1.5}$HAlBEA(I)	12.5	Calcination	1.5	13.6 ± 0.9	-
2	$Ni_{1.5}$HAlSiBEA(II)	17	Partial deallumination	1.5	86 ± 16	-
3	$Ni_{0.6}$SiBEA(II)	17	Deep deallumination	0.6	83 ± 15	-
4	$Ni_{3.0}$SiBEA(II)	17	Deep deallumination	3.0	73 ± 40	322 (275)
5	$Ni_{4.0}$SiBEA(I)	12.5	Deep deallumination	4.0	92 ± 21	329 (246)
6	$Ni_{0.7}$SiBEA(I)	12.5	Deep deallumination	0.7	150 ± 46	361 (298)
7	$Ni_{1.0}$SiBEA(I)	12.5	Deep deallumination	1.0	96 ± 15	-
8	$Ni_{1.5}$HAlBEA(II)	17	Calcination	1.5	14.5 ± 1.3	-
9	$Ni_{1.5}$SiBEA(II)	17	Deep deallumination	1.5	111 ± 14	320 (261)

The amount of Ni loaded did not significantly affect the surface area, since the BET surface area ranged from 320 and 360 m^2/g for every catalyst (Table 1).The main contribution was due to its mesopores formation (pore size less than 5 nm).

The XRD diffractograms for all the prepared samples are shown in Fig. 9. The refinement of the XRPD data was carried out by the Rietveld method [60] by using TOPAS software [61]. Through the inherent functions applied to X-ray powder

diffraction profile shape models the A, B and C polymorphs of BEA zeolite were recognised within the analyzed samples. In Table 2 the data refinements are listed; they were carried out starting from the atomic coordinates and cell parameters where the more abundant was the polymorph A (ca. 50%), followed by B (25-30%) and C (20-25%). The thermal/chemical treatment did not affect the proportion between the different crystal structures.

Table 3 reports the temperature range of reduction peaks and the relative maximum for all the samples, as detected by temperature programmed reduction-oxidation-reduction (TPR-TPO-TPR) analysis.

When a fresh sample of $Ni_{1.5}$SiBEA(II) (sample 9) was analyzed by TPR-TPO-TPR, by reducing it in one step below 450°C (TPR1, Fig. 10) a relatively sharp peak was obtained, indicating substantial homogeneity of the Ni species. Instead a rather different behavior was observed after oxidation from the second TPR run.

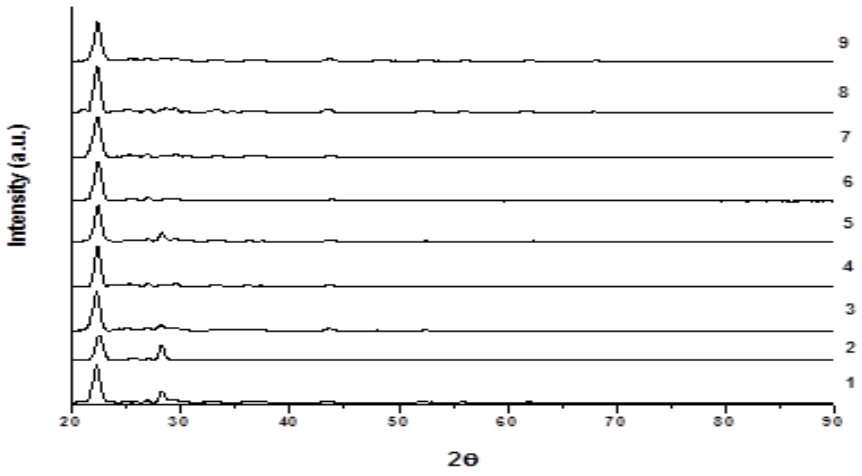

Fig. 9. XRD patterns of the prepared samples.

Two reduction peaks were present, one broad centred around 560°C and a second sharper one centred at 607°C, which evidenced stronger interaction of metal with the support after high temperature treatment. Ni was supposed to redisperse and strengthening its interaction with the support since at high temperature the reoxidation during TPO may induce the formation of Ni silicates.

Upon activation the crystal structure was kept almost unaltered and TEM confirmed that no significant sintering occurred. TPR revealed heterogeneity of the active sites because of the broaded peaks and multiple reduction features, at difference with the fresh sample.

Table 2. Rietveld elaboration of XRDP data. Quantitative distribution of the A, B and C polymorphs and relative accordance parameters R_o, r_{wp} and R_{Bragg}. The profile fitting accordance parameters describing the goodness-of-fit of the Profile. The R_{Bragg} describes the quality of the structure and the obtained crystal parametrs.

Sample	Phase	BEA A	BEA B	BEA C	R_{WP}	Rp
1	%	48.2(1)	32.4(1)	19.39(5)	3.9	3.01
	R_{Bragg}	1.77	1.62	1.99		
2	%	46.0(2)	34.8(1)	19.26(7)	4.18	3
	R_{Bragg}	1.15	0.82	1.23		
3	%	47.1(2)	33.0(1)	19.89(7)	4.62	3.61
	R_{Bragg}	1.68	1.09	1.74		
4	%	56.3(2)	24.60(9)	19.09(7)	4.41	3.32
	R_{Bragg}	1.85	1.86	1.99		
5	%	50.9(2)	29.2(1)	19.82(6)	4.24	3.27
	R_{Bragg}	1.58	1.13	1.67		
6	%	46.5(2)	35.3(1)	18.13(6)	4.24	3.27
	R_{Bragg}	1.74	1.04	1.8		
7	%	50.0(2)	30.8(1)	19.18(7)	4.53	3.51
	R_{Bragg}	1.84	1.38	1.94		
8	%	50.0(1)	33.01(9)	16.95(4)	4.44	3.55
	R_{Bragg}	1.72	1.35	1.92		
9	%	54.9(2)	25.0(1)	20.10(8)	4	3.07
	R_{Bragg}	1.62	1.59	1.72		

In previous work [18, 44-46, 56, 70-72], it was demonstrated that higher dispersion and stronger interaction with the support were evidenced by a higher reduction temperature and vice-versa. In this work we noticed that when increasing Al content, *i.e.* acidity, a decrease in the metal-support interaction strength was achieved (lower reduction temperature) when comparing samples 6,7,5 and 3,9,4. Moreover, a decrease of the reduction temperature was observed at increasing Ni content (TPR1 and TPR2 in Tab. 3), as was expected because of decreasing dispersion with increasing concentration of Ni. In addition, the high Si/Al ratio (deep dealumination) observed in sample 1 and 8 induces a shift to higher temperature of the TPR2 pattern with respect to TPR1 favored by the redispersion phenomena upon activation as was described for $Ni_{1.5}$SiBEA (II).

Table 3. Results of TPR-TPO-TPR cycles. The temperatures range of each peak is reported in the first column for each analysis and the temperatures of maximum of the peak in the second one.

	TPR1			TPO			TPR2		
Sample	**Peak(s) (°C)**	**Maximum (°C)**	**Notes**	**Peak(s) (°C)**	**Maximum (°C)**	**Notes**	**Peak(s) (°C)**	**Maximum (°C)**	**Notes**
1	227-304	267		45-85	65		320-402	343	
				85-366	187	Main peak			
2	234-275	266		30-154	77		360-515	415	
	313-425	375	Main peak				515-636	601	
3	338-440	383		57-271	72		550-652	608	Very small
4	220-271	247		29-77	58		323-479	435	
	271-411	306	Main peak	77-355	258	Main peak	479-628	582	Main peak
5	225-350	294		28-97	54		169-277	195	
				97-379	277	Main peak	277-477	378	
							477-614	569	Main peak
6	209-342	279		28-97	35		456-637	579	
	342-676	438	Main peak	97-434	213	Broad			
7	340-407	360		117-407	286		328-605	557	
	407-549		Shoulder						
8	222-300	255		29-67	50		283-472	333	
	355-550	410	Main peak	67-300	101	Main peak			
9	325-430	343		28-67	50		465-641	607	Shoulder at 553°C
				67-300	113	Main peak			

Based on the collected results, in order to improve dispersion and to strengthen the metal interaction with the support, low Ni content and high Si/Al ratio were more preferable. Then, to improve the overall stability towards coking, it is convenient to promote a low nickel reducibility, *i.e.* high dispersion and strong interaction with the support, although very low Ni content may turn into inactive catalysts.

TEM images in Fig.11 shows agglomerates of nanoparticles from 20-100 nm in size. These allow to limit mass transfer limitation inside the zeolite pores and make available most of the active sites for the reaction.

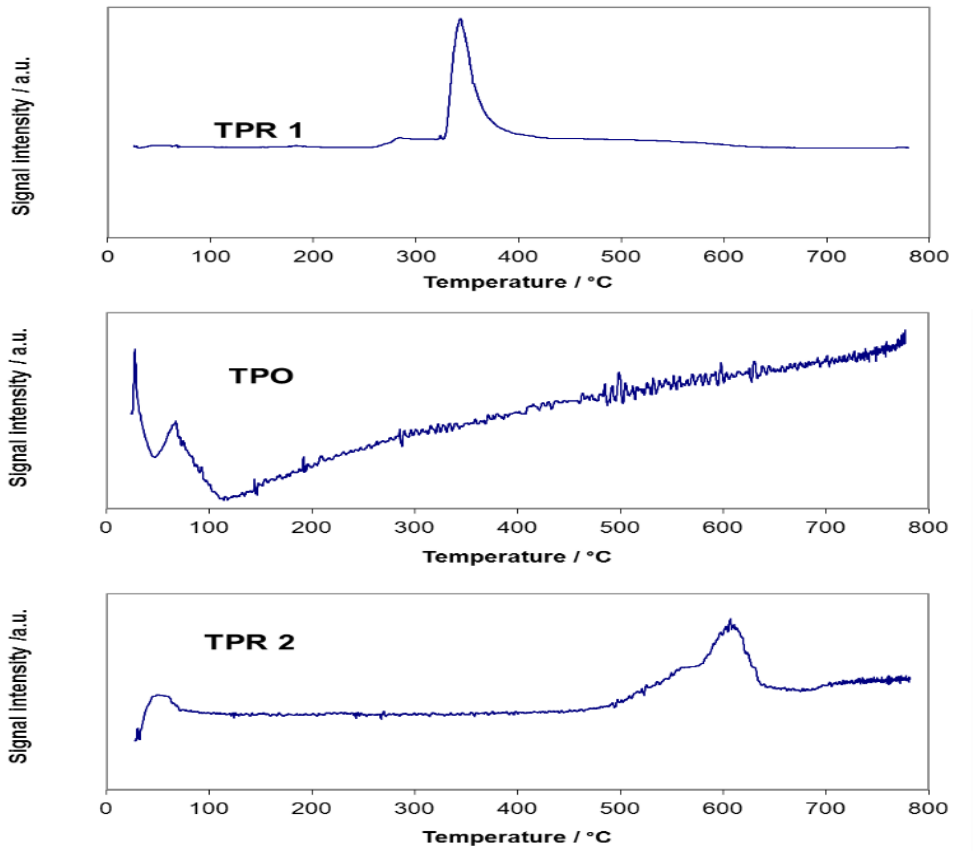

Fig. 10. TPR-TPO-TPR cycle of sample 9. The identification of Ni/NiO particles was hard also after reduction because of the low Ni content and very high dispersion. Fig. 11(a) represents the dependence of particles size on Ni loading for

both series of catalysts. Metal particles (see arrows) were visible only for samples 4 and 5 which exhibited very small Ni particle size (<5nm). Nevertheless, we also observed a strong correlation of dispersion on the Si/Al ratio (Fig. 11b). Indeed, the TPR conclusion that the highest dispersion may be reached by increasing the Si/Al content was confirmed by TEM, likely favoring the formation of a stable Ni-silicate upon activation. In samples 2 and 9 (Ni = 1.5 wt%, prepared from the two deeply dealuminated BEA) metal particles were not evident at all, whereas they were visible at the same metal loading for the two samples characterized by lower Si/Al ratio (sample 1 and 8). The reduction after activation under H_2 flow at 800°C for sample 1 (Fig 11c) completely vanished the Ni particles found in Fig. 11b, confirming the hypothesis of Ni redispersion upon activation.

FTIR spectra of BEA surface and probe molecules adsorption have been performed. The spectra of pure samples 1, 2, 3 and 8, 9 are reported in Fig. 12 in common scale, recorded after outgassing at 500°C, focusing on the OH stretching region. The spectra of samples 1 and 8 (calcined samples) are characterised by a quite complex pattern of bands, consisting of a main adsorption at 3740 cm^{-1}, possibly complex, and by two weak components at 3670 and 3605 cm^{-1}, completely consistent with the spectra reported for H-BEA materials after calcination [73-76]. We assigned the main band to the stretching mode of terminal

a)

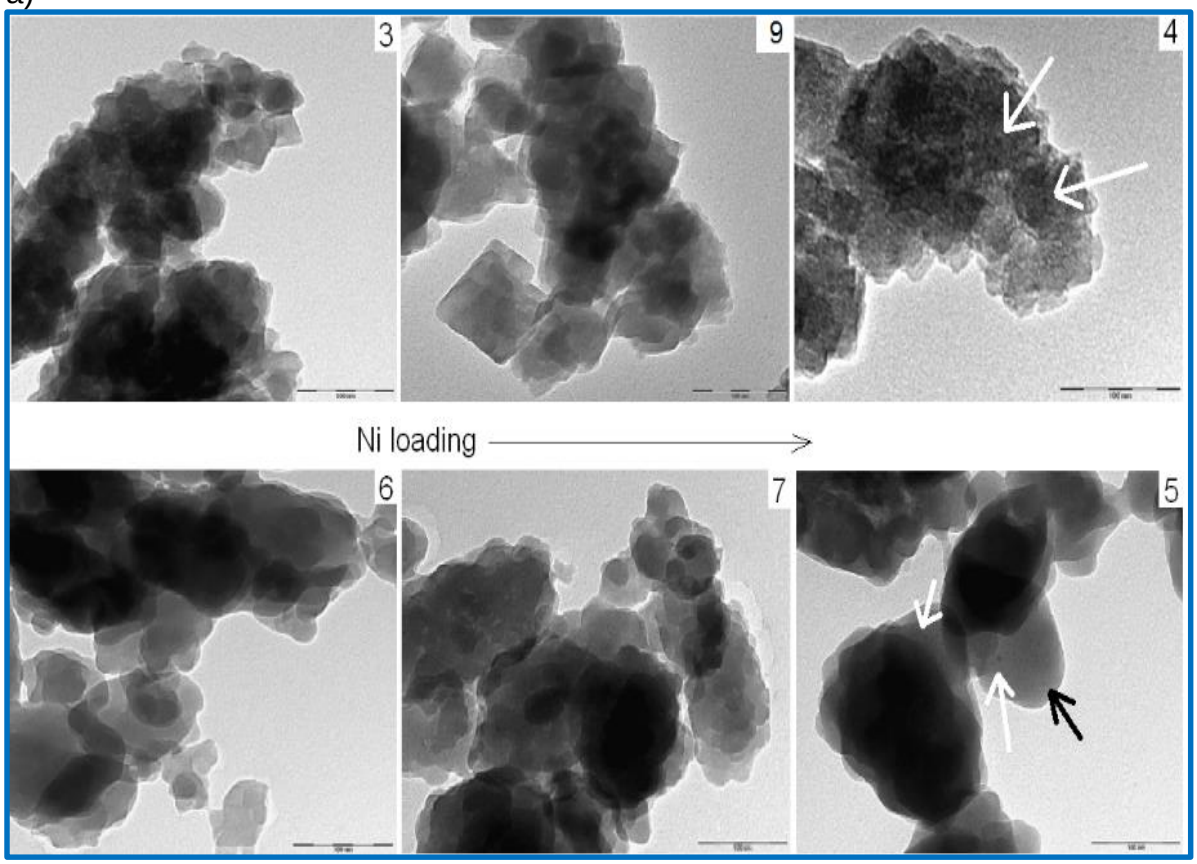

b)

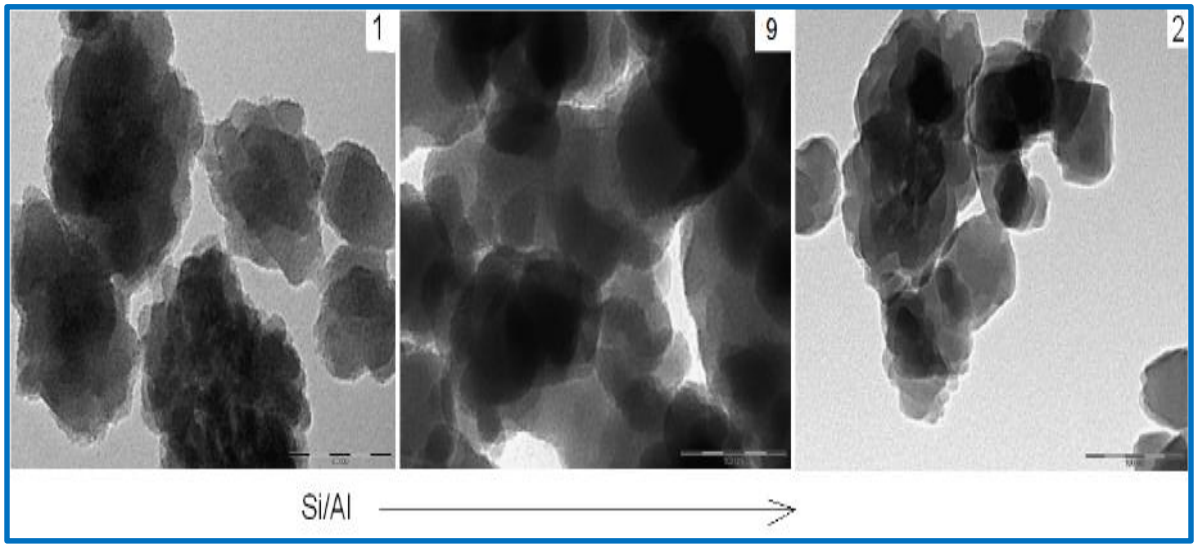

c)

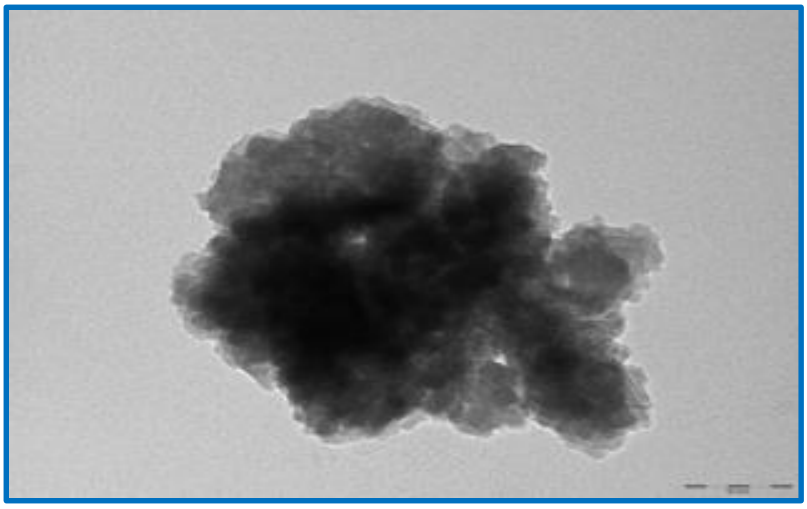

Fig. 11. TEM micrographs of samples with a) variable Ni loading, b) variable Si/Al ratio, c) sample1 reduced at 800°C. Marker size 100 nm. Ni particles evidenced arrows when needed.

Si-OH groups to be located mainly at the external crystal surface. Its complexity should arise from the formation of two different families of silanol groups.

The band at 3605 cm^{-1} was assigned to bridging Al-OH-Si groups commonly associated to the Brønsted acidity of these materials, in particular to OHs in the internal sinusoidal channels of H-BEA [74], whereas the component at 3670 cm^{-1} was assigned to Al-OH groups of Al ions in extraframework position.

The detection of a very weak band at 3780 cm^{-1} suggests that also another kind of Al-OH extraframework species were formed, having different coordination states.

The spectrum of sample 8 showed a shaper component at 3739 cm^{-1}, without the enlargement detected for the sample 1 peaks. This evidenced the formation of a single type of silanol groups over the catalyst surface. Moreover, it can be noticed

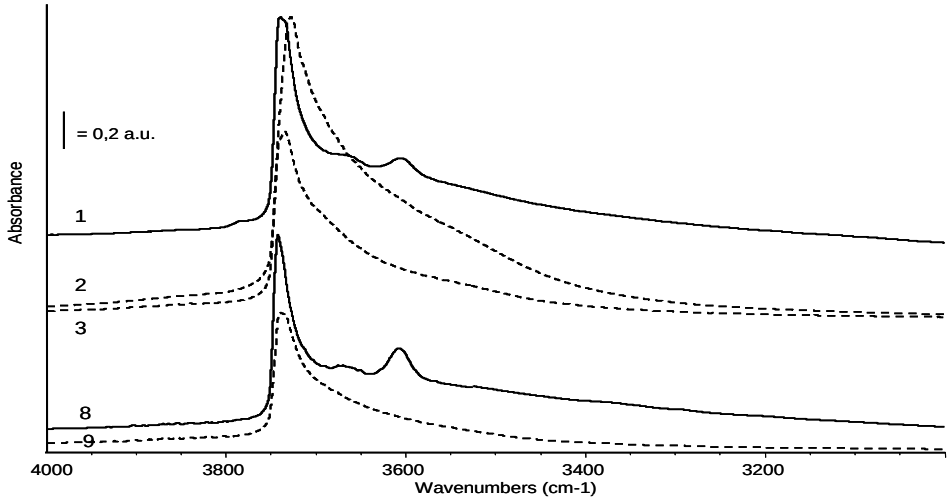

Fig. 12. FT IR spectra of samples 1, 2, 3, 8 and 9 after outgassing at 500°C. OH stretching region.

that sample 8 spectrum is lacking of the high frequency band, assigned to extraframework Al. Therefore, in spite of the similar Si/Al ratio (Table 1), a starting material with lower Al allows its better allocation into the framework.

In this spectral region, for samples 2, 3 and 9 (after dealumination treatment) only one main band centred at 3730 cm^{-1} was found, clearly formed by two components and tailing to lower frequencies, while the components below 3700 cm^{-1} disappeared. In particular, the disappearance of the band at 3605 cm^{-1} due to the

observed disappearance of the Brønsted acidity. This effect points out the dealumination strongly affecting the framework structure [74, 75]. Moreover, deep dealumination (samples 3 and 9) led to a reduction of the overall OH bands intensity.

Therefore, FT IR spectra, confirms that the extended dealumination of samples 2, 3 and 9 changed the amount and the nature of surface acidic sites. In fact over these samples Brønsted acidity disappeared as well as the strongest Lewis sites.

3.2 Activity testing for Steam Reforming of Ethanol

The catalytic activity of these samples was tested for the steam reforming of ethanol at 750°C. The results have been collected in the following tables:

Table 4: Results of activity testing at 750°C, GHSV= 1700 h^{-1} , H_2O/CH_3CH_2OH=3mol/mol, if not else specified. Focus on catalyst acidity.

750°C	9	2	8	1	1 *
CO/CO_2	11.7 ± 1.1	-	46 ± 2	30.1 ± 1.2**	n.d. ***
C balance (%)	99 ± 3	98 ± 4	99 ± 4	99 ± 2	100 ± 1
Conv. H_2O (%)	47 ± 7	-	42 ± 12	46 ± 9	30 ± 2
Conv. EtOH (%)	100	100	100	100	100
H_2 productivity (mol/min kg_{cat})	0.73 ± 0.08	0.94 ± 0.02	0.72 ± 0.03	0.61 ± 0.09	0.61 ± 0.09
S_{CH3CHO} (%)	-	2.4 ± 0.3	-	-	-
S_{CH4} (%)	5.9 ± 0.3	1.9 ± 0.3	4.8 ± 0.8	4.8 ± 0.5	4.7 ± 0.4
S_{C2H4} (%)	-	-	-	-	10 ± 2
Notes					
* contact time = 3655 h^{-1}					
** CO/CO_2 decreased to 6.6 ± 0.7 decreasing temperature to 625°C					
*** CO_2 not detected during the whole test					

Table 5. Results of activity testing at 750°C, GHSV= 1700 h^{-1} ,H_2O/CH_3CH_2OH=3 mol/mol, if not else specified. Effect of Ni content.

	Initial Si/Al = 17 (atom/atom) + deep deallumination			Initial Si/Al = 12.5 (atom/atom) + deep deallumination		
750°C	**3**	**9**	**4**	**6**	**7**	**5**
CO/CO_2	38 ± 5*	11.7 ± 1.1	3.9 ± 0.3	39 ± 6	18 ± 1	2.4 ± 0.3
C balance (%)	99 ± 2	99 ± 3	99 ± 4	98 ± 2	96 ± 2	97 ± 4
Conv. H_2O (%)	35 ± 2	47 ± 7	52 ± 4	25 ± 3	41 ± 10	57 ± 7
Conv. EtOH (%)	100	100	100	100	100	100
H_2 productivity (mol/min kg_{cat})	0.73 ± 0.03	0.73 ± 0.08	0.82 ± 0.03	0.70 ± 0.04	0.79 ± 0.03	0.87 ± 0.08
S_{CH3CHO} (%)	-	-	-	-	-	-
S_{CH4} (%)	8 ± 3	5.9 ± 0.3	3.8 ± 0.6	6.5 ± 0.4	6.4 ± 0.3	3.5 ± 1.5
S_{C2H4} (%)	1.2 ± 1.1	-	-	2.5 ± 1.7	-	-
Notes						
* CO/CO_2 decreased to 18 ± 2 at 625°C but the selectivity to ethylene and aceteldehyde increased to 39% and 13%, respectively						

Considering the different acidity, *i.e.* samples $Ni_{1.5}$HAlBEA(I), $Ni_{1.5}$HAlSiBEA(II), $Ni_{1.5}$HAlBEA(II), and $Ni_{1.5}$SiBEA(II) (catalysts 1, 2, 8 and 9) and the same Ni content (1.5 wt%), but different Si/Al ratio, we searched for a correlation between the acidity and catalytic activity (table 4).

Based on the Si/Al ratio (Table 1) and on the depth of dealumination treatment, the following acidity scale was expected, perfectly confirmed by FT-IR analysis: 1 ($N_{1.5}$HAlBEA(I), strong Brønsted acidity, mainly), > 8 ($Ni_{1.5}$HAlBEA(II), strong Brønsted acidity, mainly) > 2 $Ni_{1.5}$HAlSiBEA(II), traces of Brønsted acidity), > 9 ($Ni_{1.5}$SiBEA(II) acidity substantially suppressed). This is in the line with the Al content, decreasing in this order.

As result for activity testing under the specified reaction conditions at 750°C, all the samples showed full ethanol conversion. Some CH_4 formed by ethanol

decomposition and it was not completely reformed. Since this set of sample was poorly active for the water gas shift (WGS) reaction, the H_2 productivity was not the highest achievable. Moreover, CO_2 was almost absent in the product distribution and the selectivity to CO and H_2 was almost equal. The low Ni loading of these samples (see above) seem to favor this products distribution. This leads to optimal H_2/CO ratio for the production of chemicals through the Fischer-Tropsch (FT) reaction rather than for H_2 valorisation as fuel. Sample 2 $N_{1.5}$HAlSiBEA(II) showed higher activity for the WGS reaction, leading to the highest H_2 productivity within this set of samples. This may be an interesting result if the main goals is the production of H_2, but induces a misbalance between CO and H_2 selectivities if the purpose is the FT valorisation of the syngas produced from ethanol. In any case, the CO/CO_2 ratio may be also tuned by modifying temperature. For instance, sample 1 $Ni_{1.5}$HALBEA(I) tested at 625^{o}C led to CO/CO_2 = 6.7 ± 0.6 (mol/mol) with increase of H_2 yield, since lower temperature favored the WGS equilibrium.

As expected, the C balance was around 100% for every sample tested at 750 and 625^{o}C, irrespectively of acidity. Indeed, at such high temperature the carbon deposits possibly accumulated over the catalyst surface may be easily gasified. In general, the performance of this set of catalyst was rather similar, suggesting that acidity does not play a key role when operating steam reforming at high temperature. By lowering the contact time (GHSV = 3655 h^{-1}), another test to check the acidity effect was performed on sample 1 $Ni_{1.5}$HALBEA(I), *i.e.* the most acidic one, thus in principle more critical as for deactivation by coking related to acidity. The results showed the massive formation of ethylene, which was not

effectively reformed at decreased contact time. Thus, increased acidity favors the ethanol dehydration pathway to form ethylene as expected. Nevertheless, the complete carbon balance at reactor outlet did not suggest any extensive ethylene polymerization and subsequent coke accumulation over catalyst surface under these reaction conditions.

Focusing on the effect of Ni loading (table 5), a native Si/Al =17 was used, followed by deep dealumination (samples 3 $Ni_{0.6}$SiBEA(II), 9 $Ni_{1.5}$SiBEA(II) and 4 $Ni_{3.0}$SiBEA(II), the subscript after Ni indicating its loading in wt%), whereas a second series was prepared from the BEA structure originally containing SI/Al = 12.5, followed also in this case by deep dealumination (samples 6 $N_{0.7}$SiBEA(I), 7 $Ni_{1.0}$SiBEA(I) and 5 $Ni_{4.0}$SiBEA(I)). In this case, we may consider the effect of acidity as limited for the conlusions above reported. Results of activity testing are reported in Table 5. As expected in virtue of the high operating temperature, the first group of samples tested at 750ºC, exhibited similar C balance and ethanol conversion of 100% in every case. However, in contrast to acidity, Ni loading deeply affected product distribution. H_2 productivity increased with Ni content and correspondingly the CO/CO_2 ratio decreased. These two parameters are of course correlated, since they both suggest increasing activity for the steam reforming and WGS reactions with increasing metal loading.

More precisely, at the lowest Ni loading unreformed ethylene was present even at such a high temperature, but it was completely reformed for the samples with the highest Ni loadings. Accordingly, some unreformed methane was still present for every sample, but its selectivity systematically decreased with increasing

concentration of the active phase. The 100% C balance also suggests that even if ethylene formed, it did not accumulate over the poorly acidic sites. It was completely reformed at high temperature provided that enough Ni was present.

By looking at Fig. 13 one may observe that both the selectivity to CH_4 and the CO/CO_2 ratio decreased with increasing Ni content, index of increasing reactivity for the methane steam reforming and WGS reactions, respectively. The trends clearly reached a plateau value at 3-4 wt% Ni, sufficient to ensure satisfactory activity for this application. Since water conversion and H_2 productivity increase with Ni loading a similar conclusion may be inferred. Moreover, to increase activity for H_2 production the Ni loading should be increased to 10 wt%. Indeed, this sample led to CO/CO_2 =2.9 (mol/mol) and completely converted methane, so enhancing hydrogen productivity, but leading to an unbalanced reaction mixture for the FT reaction.

No significant stability issues were evident at this operating temperature and the C balance was satisfactory for each catalyst.

The same results have been achieved when testing samples 6 $Ni_{0.7}$SiBEA(I), 7 $Ni_{1.0}$SiBEA (I), 5$Ni_{4.0}$SiBEA(I) prepared with variable Ni loading, but with an initial Si/Al ratio = 12.5, followed by dealumination (Table 5, Fig. 13 and 14).

Some conclusions on the reducibility of Ni oxide and on the strength of interaction between the metal and the support can be mentioned based on the TPR-TPO-TPR cycles. As above recalled, the highest the reduction temperature, the strongest

such interaction. Provided that the metal and the support are the same, this usually means higher Ni dispersion.

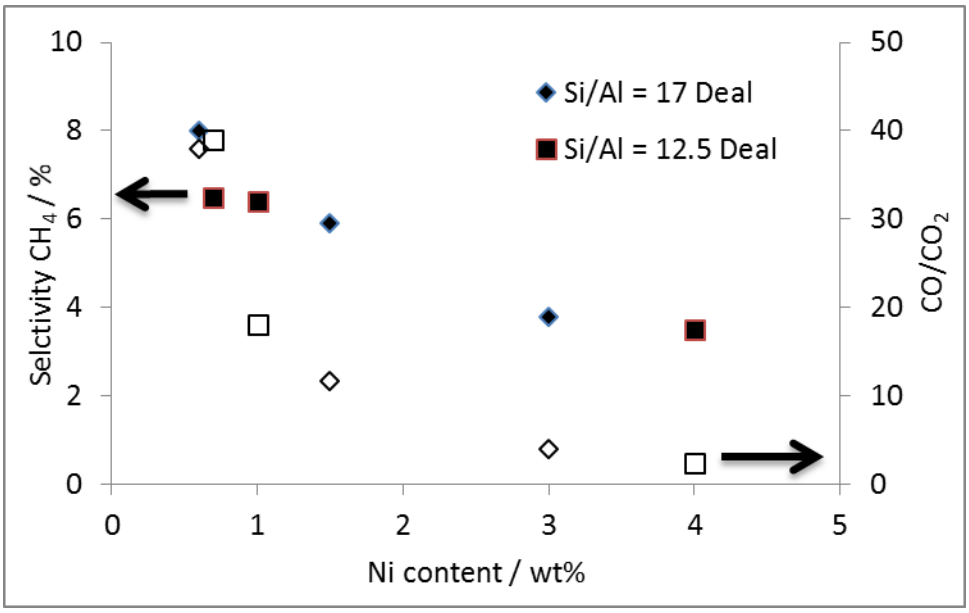

Fig. 13. Effect of Ni loading on selectivity to CH_4 (full symbols, left axis) and activity for the WGS reaction (empty dots, right axis).

For the series of samples 3 $Ni_{0.6}$SiBEA(II), 9 $Ni_{1.5}$SiBEA(II), 4 $Ni_{3.0}$SiBEA(II) a reduction peak was observed between 300 and 400°C in the TPR of the fresh catalyst (Table 3). Peak intensity increased with Ni loading and the reduction temperature slightly decreased. Same behavior of decreasing dispersion with Ni content was observed for the series of samples 6 $Ni_{0.7}$SiBEA(I), 7 $Ni_{1.0}$SiBEA(I), 5 $Ni_{4.0}$SiBEA(I), with higher decrease between each reduction temperatures at increasing the Ni loading compared with the previous group of catalysts

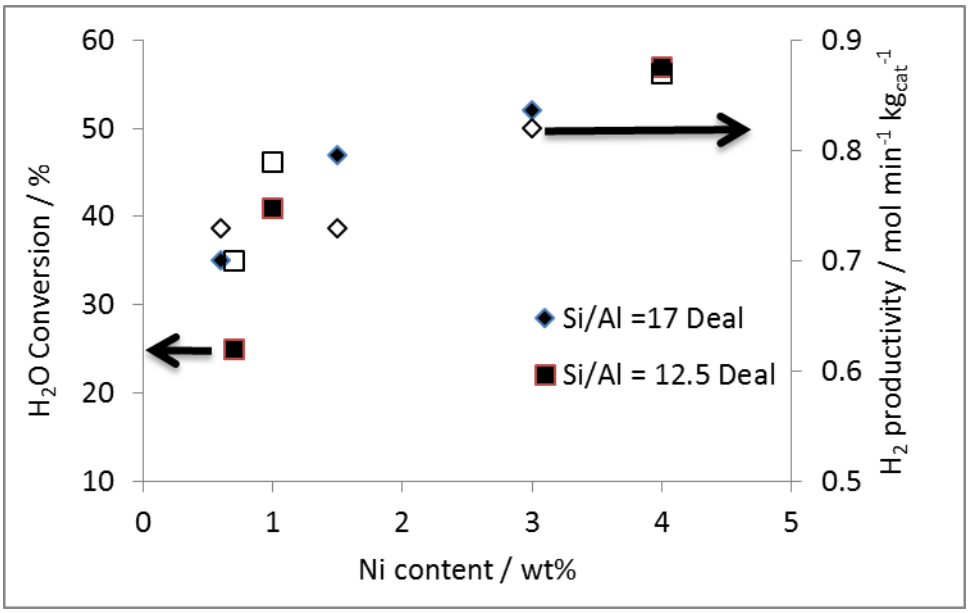

Fig. 14. Effect of Ni loading on the conversion of H_2O (full symbols, left axis) and H_2 productivity (empty dots, right axis).

3.3 Summary

The preparation of Ni-based catalysts supported over BEA zeolite was carried out and tested for SRE. The catalyst performance resulted affected by variation on Ni loading and Si/Al ratio.

Although at high temperature (625-750ºC) the activity testing was characterized by full ethanol conversion, at low Ni loading unreformed by-products were still present. The increase of Ni loading improved the catalytic activity for the steam reforming of methane and for the water gas shift reaction, reaching higher H_2 productivity. Sensitive factor for catalyst acidity was the Si/Al ratio, but at high temperature operation, the effect was lower. The dealumination treatments led to poor residual acidity which provoked the elimination of the strong Brønsted and Lewis acidic

sites. It means that by controlling the catalyst acidity towards Si/Al ratio of the support may be suppressed the deactivation by coking.

3.4 Characterization of Ni/La_2O_3 and Ni/TiO_2 catalysts

As second catalyst formulation was proposed to study the effect of metal active phase loading on SRE. Ni catalysts supported over lanthana and titania with different metal content were prepared as described in Chapter 2. The following characterization results were achieved.

Textural, structural and morphological characterization.

The composition and synthesis method for all the samples is summarized in Table 6.

The samples were characterized by different specific surface area (SSA), depending on the support. SSA was 84 and 41 m^2/g for TiO_2 and La_2O_3, respectively. After deposition of the active phase by impregnation the SSA dramatically decreased. By contrast, samples made directly by FP showed SSA comparable with the respective support in the case of lanthana support, decreased by ca. 30% in the case of TiO_2 supported samples.

EDX analysis allowed to check catalysts composition. The results showed a higher atomic ratio of Ni/La respect to Ni/Ti for both the FP-made and impregnated samples, as expected from nominal composition. However, the samples prepared

in one step by FP were characterized by lower Ni/(La,Ti) ratios than those prepared by impregnation. EDS analysis is not properly a surface-sensitive tool, but it does not have high in-depth sensitivity. In this light, we can confirm higher surface exposure obtained by impregnation of the active phase than by one step synthesis. This in turns means a higher Ni dispersion in the support matrix for the FP-prepared samples. Furthermore, due to high stability of the $LaNiO_3$ mixed oxide, it was hard to keep NiO segregated on the surface when supported over La_2O_3.

Table 6. Composition and main properties of the samples. SSA= specific surface area from BET regression of N_2 adsorption/desorption data. Actual Ni/Ti or La molar ratio from EDX analysis.

Sample	Composition	SSA (m^2/g)	Ni/Ti or La (mol/mol)
Ti-F	TiO_2	84	-
La-F	La_2O_3	41	-
5-Ni/Ti-I	5wt% Ni /TiO_2	-	0.09
10-Ni/Ti-I	10wt% Ni /TiO_2	6.4	0.12
15-Ni/Ti-I	15wt% Ni /TiO_2	-	0.30
5-Ni/Ti-F	5wt% Ni /TiO_2	55	0.05
10-Ni/TI-F	10wt% Ni /TiO_2	62	0.13
15-NI/Ti-F	15wt% Ni /TiO_2	53	0.16
5-Ni/La-I	5wt% Ni /La_2O_3	-	0.29
10-Ni/La-I	10wt% Ni /La_2O_3	11	0.58
15-Ni/La-I	15wt% Ni /La_2O_3	-	0.62
5-Ni/La-F	5wt% Ni /La_2O_3	48	0.12
10-NI/La-F	10wt% Ni /La_2O_3	42	0.32
15-Ni/La-F	15wt% Ni /La_2O_3	40	0.52
LaNi-F	$LaNiO_3$	11	1.09

The TiO_2 sample showed a highly crystalline structure composed of rutile and anatase, the latter being the main component (whereas La_2O_3 was constituted by the highly hydrated form $La(OH)_3$ only. Ni addition during the FP synthesis modified the crystal structure of the support and rutile became the predominant phase (Fig.

15), the only one after sample activation by reduction at 800°C. Similar results were achieved for the impregnated samples and at different Ni loading (Fig. 16). We did not get significant evidence of reflections attributed to Ni oxides or metallic Ni in the fresh samples, whereas Ni reflections appeared in the activated samples and their intensity increased as expected with loading. Furthermore, metal dispersion was higher in the case of the samples prepared one-pot by FP than for the impregnated ones.

Fig. 15. XRD patterns of TiO_2 based samples. From bottom up: Ti, 15-Ni/Ti-Fand 15-Ni/Ti-F after activation.

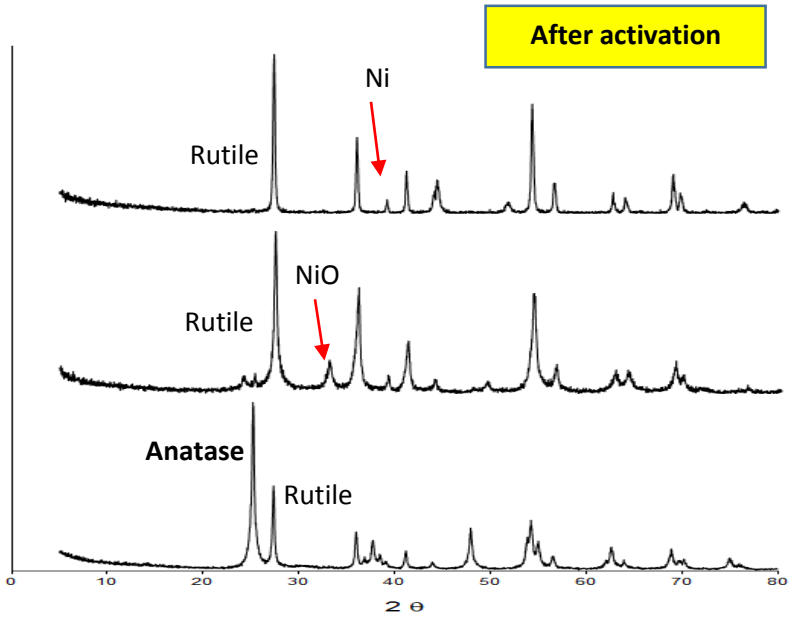

Christensen et al. [39] demonstrated the importance of the crystallite size of Ni for the steam reforming of methane and we already discussed in the previous paragraphs the importance for SRE activity and resistance to deactivation.

After the addition of the active phase to the FP made lanthana, a lot of new reflections appeared that could be attributed to NiO, mainly as mixed oxide with the support: La_2NiO_4, NiO/ La_2NiO_3 (Fig. 17). After reduction, La $(OH)_3$ became the main phase, even with $LaNiO_3$, while La_2NiO_4 almost disappeared and the reflections of metallic nickel became more intense. The formation of mixed oxide may be the key parameter to keep the metal well dispersed on the support, thus limiting coking activity.

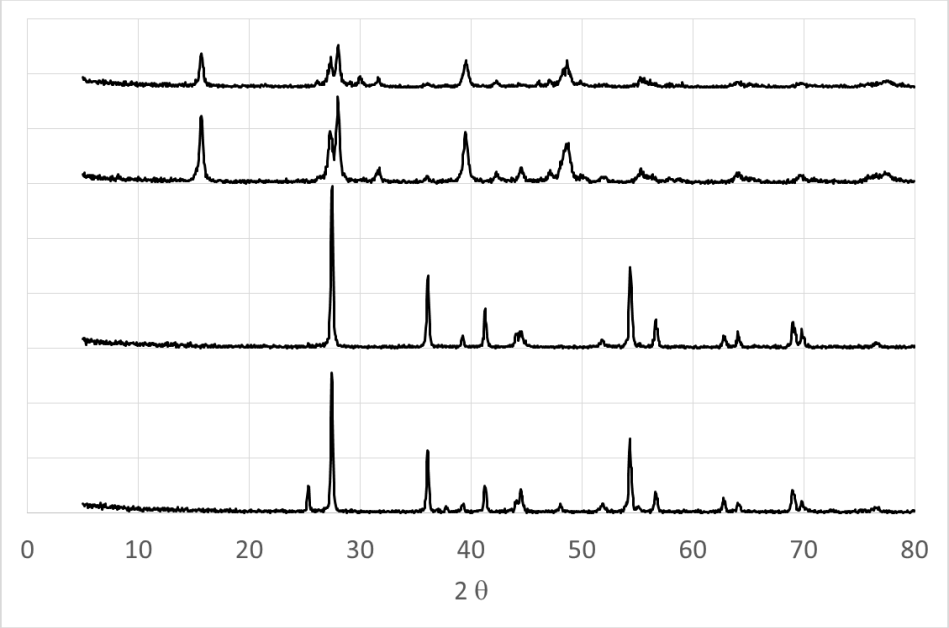

Fig. 16. XRD patterns of activated samples. From bottom up: 10-Ni/Ti-I, 10-Ni/Ti-F, 10-Ni/La-I, 10- Ni/La-F.

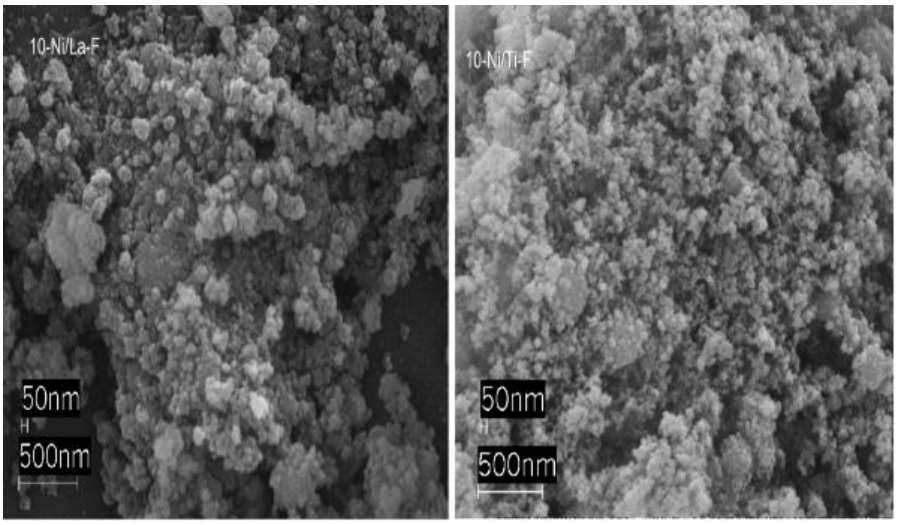

Fig. 17. Typical SEM micrograph images of FP-made samples

SEM micrographs (Fig. 17) of all the samples show that they were composed of uniformly sized agglomerates (*ca.* 50 nm). Their primary particles were much smaller as observed by TEM analysis (Fig.18), but different depending on the support and preparation method. The lanthana support was constituted by uniform nanoparticles, *ca*. 20 nm in size, but the high hydration degree (see XRD) induced agglomeration during impregnation, as testified by the TEM picture of sample 5-Ni/La-I. Similar images were obtained at higher Ni loading. This phenomenon was not observed for the samples synthetised in one step (e.g. 5-Ni/Ti-F in Fig. 18). On the contrary, a bit smaller (10-20 nm) and uniform particle size was observed for all the TiO_2 supported samples, irrespectively of the Ni loading and preparation method.

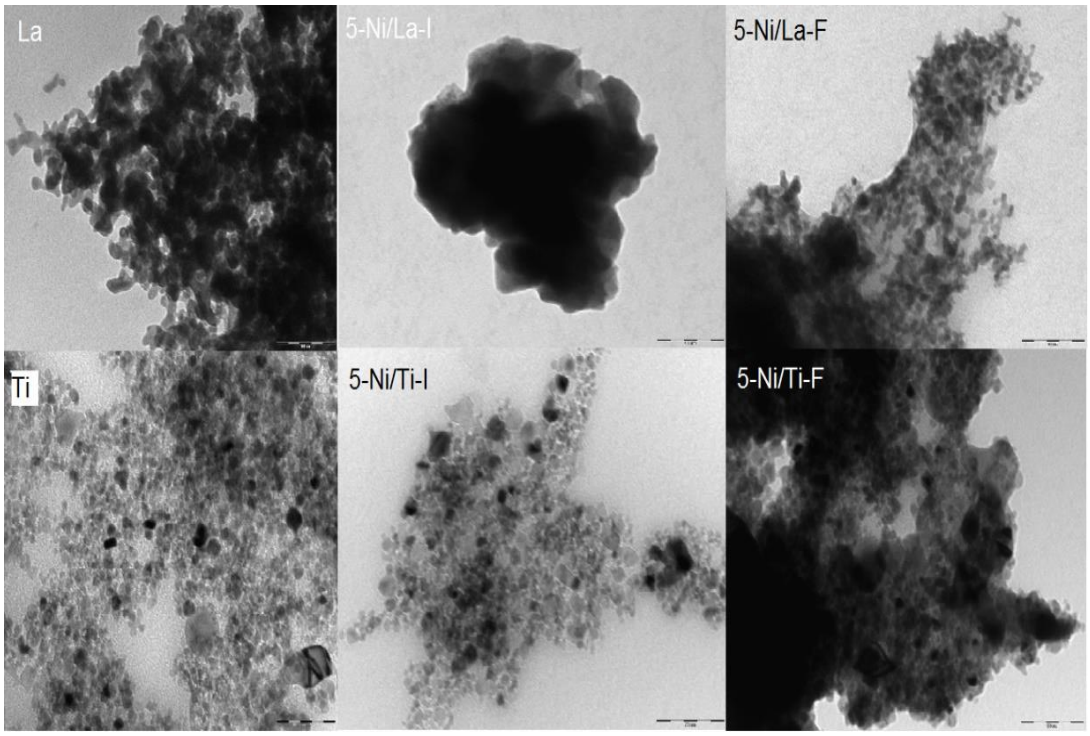

Fig. 18. TEM micrographs of selected samples. Marker size: 100 nm

Temperature Programmed Reduction

TPR analysis was carried out to determine the reduction temperature of Ni ions for each sample. As reported in previous investigations, this parameter was an important indication of the metal-support interaction strength. In particular, for a given metal and support couple, the highest the reduction temperature, the strongest the metal support interaction and/or the metal dispersion. Smallest particle size was also usually correlated to a lowest coking rate [44].

TPR patterns of significant samples are reported in Fig. 19-21. The H_2 consumption of 15 wt% Ni supported over TiO_2 are reported in Fig. 20 for differently prepared catalyst. Lower reducibility was observed for the FP prepared samples with respect to the impregnated ones. This is commonly ascribed to higher dispersion, which is

indeed imparted by the one pot synthesis with respect to impregnation. Higher reducibility was also observed for the TiO_2 supported samples, with respect to lanthana-based ones, especially when prepared by impregnation. This denotes a stronger metal-support interaction between NiO and La_2O_3, in case also leading to mixed-oxide formation (harsher reducibility), as observed indeed by XRD.

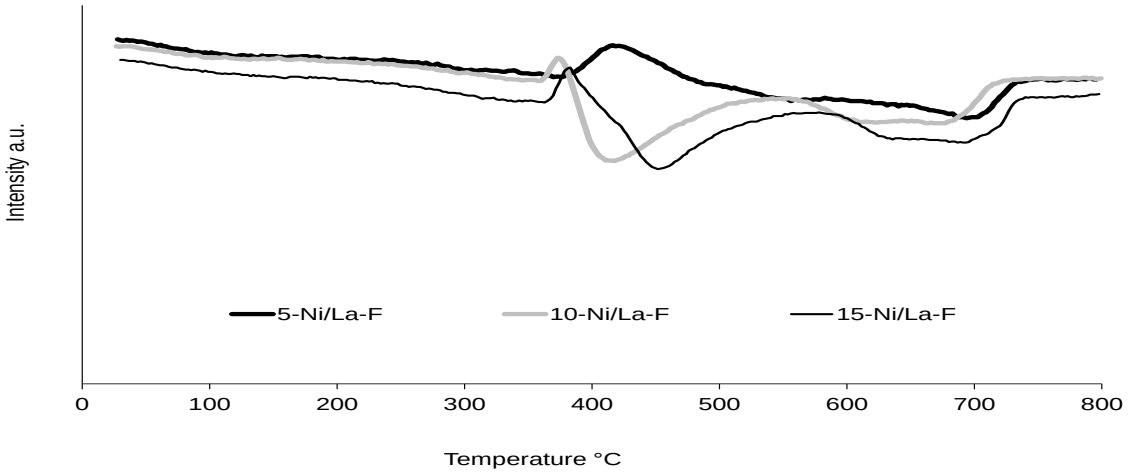

Fig. 19. TPR patterns of differently supported lanthana-and prepared samples. MS Signal intensity referred to H_2 consumption.

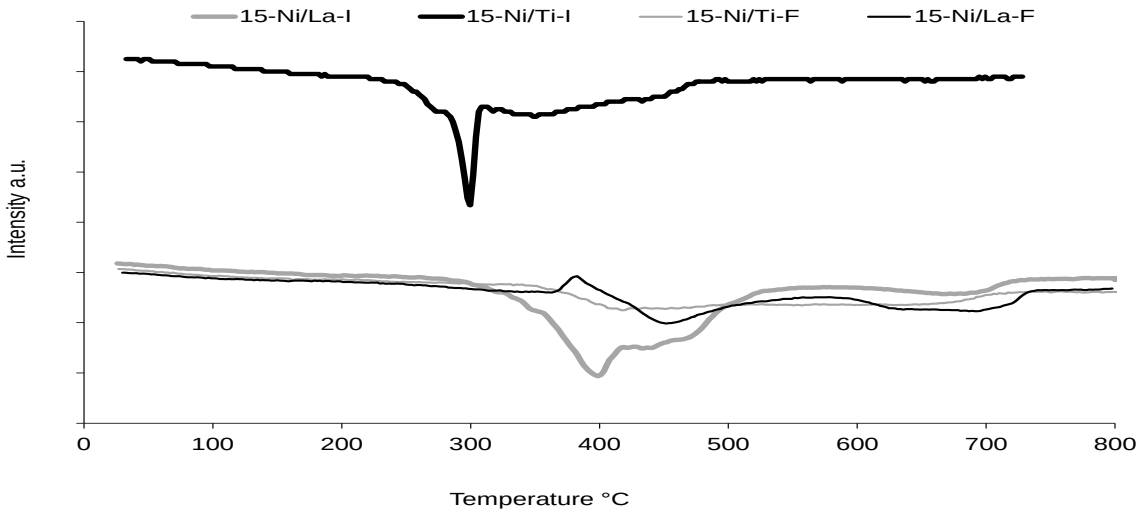

Fig. 20. TPR patterns of supported samples prepared by FP. MS signal Intensity referred to H_2 consumption.

Increasing metal loading determines increasing H_2 consumption (Fig. 19), but substantially similar reduction temperature in the case of the impregnated samples. This denotes a quite similar NiO dispersion, which is expected to be reasonably low due to relatively high loading on supports with moderate surface area. By contrast, the one-pot synthesis led to slightly higher reduction temperature with increasing Ni loading (Fig. 20). This was ascribed to the formation of an increasing amount of mixed oxide, as detected also by XRD.

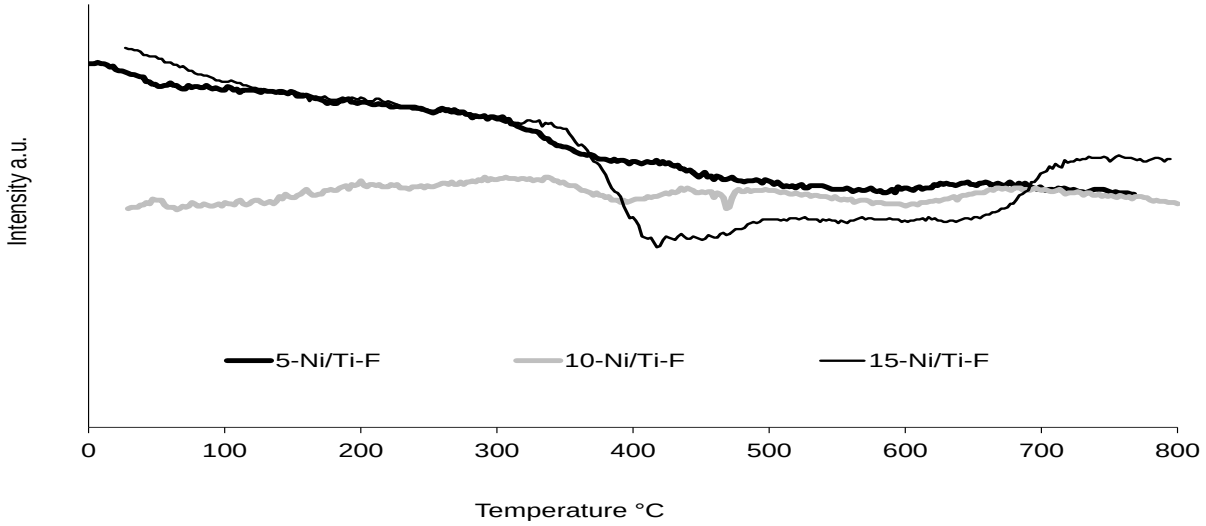

Fig. 21. TPR patterns of titania-supported samples prepared by FP. MS signal intensity referred to H_2 consumption.

3.5 Activity testing for Steam Reforming of Ethanol

When tested the samples at 750^{o}C every sample showed full ethanol conversion and negligible formation of carbon deposits, as testified by the C balance *ca.* 100% (Table 7). The FP-prepared samples were usually characterized by a higher H_2 productivity due to slightly higher water conversion. The reason can be searched in the intimate contact between the metal particles and the support, which is responsible of water activation. Thus, a more dispersed active phase can enhance the utilisation of activated OH and H species to complete conversion into reformate gas. The superior catalytic activity of the FP samples is also evident for the steam reforming of methane. In this context, methane is formed by ethanol decomposition and its reforming is favored by the good Ni dispersion here achieved, as evidenced by XRD and TPR. High metal loading is needed with the impregnated samples to achieve complete methane conversion (as reported also with the Ni-BEA catalyst series), whereas no methane outflow was observed with the FP prepared samples even at low loading. The higher Ni dispersion and metal support interaction accounts also for this point.

Overall, the H_2 productivity ranged between 1.7 and 2.3 mol/min $Kg_{cat.}$ Assuming the use of the reformate to feed a PEM fuel cell with *ca*. 40% efficiency towards electrical energy, the catalyst amount needed to feed a $5Kw_{el}$ device would be

1.35-1.8 kg.

Table 7. Activity testing at 750°C, water/ethanol= 3 (mol/mol), GHSV= 2500 h^{-1}. S= selectivity.

Catalyst	C balance (%)	H_2 productivity (mol/min)/ kg_{cat}	Ethanol Conversion (-)	S CH_3CHO (%)	S CH_4 (%)
5-Ni/La-F	**103±4**	**1.93±0.10**	**1.0**	**0**	**0**
5-Ni/La-I	**103±3**	**1.8±0.2**	**1.0**	**0**	**0.7 ± 0.2**
5-Ni/Ti.F	**105±6**	**2.07±0.14**	**1.0**	**0**	**0.9 ± 0.2**
5-Ni/Ti-I	**99±3**	**1.7±0.2**	**1.0**	**0**	**1.2 ± 0.3**
10-Ni/La-F	**100.0±1.4**	**2.05±0.03**	**1.0**	**0**	**0**
10-Ni/La-I	**102±2**	**1.85±0.02**	**1.0**	**0**	**1.05 ± 0.12**
10-Ni/Ti-F	**100±3**	**1.40±0.03**	**1.0**	**0**	**0**
10-Ni/Ti-I	**95.4±1.7**	**1.77±0.10**	**1.0**	**0**	**0**
15-Ni/La-F	**98±4**	**1.85±0.10**	**1.0**	**0**	**1.2 ± 0.3**
15-Ni/La-I	**99±7**	**2.3±0.5**	**1.0**	**0**	**0**
15-Ni/Ti- F	**100.4±1.8**	**2.12±0.14**	**1.0**	**0**	**0**
15-Ni/Ti-I	**101±2**	**2.0±0.1**	**1.0**	**0**	**0**
LaNi-F	**101±7**	**1.9±0.2**	**1.0**	**0**	**0**

This is a conservative estimation without taking into account the additional H_2 production through water gas shift reactors, usually connected in series to the reformer in commercial devices.

With the aim of process intensification, it is desirable to lower the steam reforming temperature to limit the heat load to the reactor [77], but at such low temperature coke accumulations is not effectively counter balanced by its removal by steam gasification [78]. This may induce rapid catalyst deactivation by formation of encapsulating coke or carbon nanofilaments [72]. The C balance is an effective parameter to monitor possible coke accumulation under these reaction conditions, as extensively described elsewhere [73].

The results of activity testing at 500°C are summarised in Table 8. Both the FP and impregnated catalysts prepared over lanthana with the lowest Ni loading (5-10 wt%) did not reach a satisfactory ethanol conversion. Non negligible selectivity to acetaldehyde was also observed, together with incomplete methane reforming, overall depressing H_2 productivity.

C balance (blank test at 500°C returned 91 ± 4%) was generally higher for the FP prepared samples, coupled with a good durability with time-on-stream. As above mentioned this is ascribed to the higher dispersion of Ni and its strong metal-support interaction. High Ni loading is needed to attain full ethanol conversion and no C_2 by products in the outlet gas at such a low reaction temperature.

By comparing the two supports, contrasting effects were evident. On one hand, TiO_2 usually led to higher activity (*i.e.* superior ethanol conversion, lower selectivity to acetaldehyde and methane) [75, 76]. On the other hand, the different acid-base character of the support and different ability to disperse and stabilize the active phase induced a remarkable difference in the resistance toward coking, being La_2O_3 much more preferable from this point of view due to its basic character. Higher Ni dispersion was also attained when supported over La_2O_3, especially when prepared by FP. This is another reason for higher resistance to coking imparted by the smaller Ni particle size, due to lower formation of C nanofilaments. In this sense, the excessive Ni loading achieved with $LaNiO_3$ was detrimental for coking activity. Indeed, in spite of the 1:1 ionic dispersion in the precursor, after activation the high Ni concentration led to unavoidable decrease of dispersion. This in turn determined a decreasing C balance.

Table 8. Activity testing at 500°C, water/ethanol= 3 (mol/mol), GHSV = 2500 h^{-1}.

Catalyst	C balance (%)	H_2 productivity (mol/min)/ kg_{cat}	Ethanol Conversion (-)	S CH_3CHO (%)	S CH_4 (%)
5-Ni/La-F	96±8	0.88±0.09	0.6±0.2	12± 5	8.5*
5-Ni/La-I	67±8	0.6±0.2	0.66±0.06	9.1±0.5	1.3±0.3
5-/NiTi-F	75±4	1.6±0.2	1.0	0	4.8±0.2
5-Ni/Ti-I	58±5	1.07±0.07	1.0	3.7±1.4	2.3±0.4
10-Ni/La-F	89±2	1.18±0.05	0.72±0.05	7.4±0.2	6.7±0.3
10-Ni/La-I	93±4	1.42±0.07	0.97±0.04	3.7±0.4	9.7±0.7
10-Ni/Ti-F	82± 8	0.90±0.06	1.0	2.5±0.9	3.5±0.3
10-Ni/Ti-I	75±8	1.4±0.2	1.0	0	12.5±1.6
15-Ni/La-F	95±2	1.75±0.02	1.0	0	9.8±0.3
15-Ni/La-I	78±5	1.8±0.4	1.0	0	4.9±1.9
15-Ni/Ti-F	61±2	1.44±0.05	1.0	0	3.5±1.0
15-Ni/Ti-I	69±3	1.67±0.02	1.0	0	5.0±0.6
LaNi-F	83.3±0.8	1.69±0.08	1.0	0	7.3±0.2

It can be overall concluded that, based on the highest C balance and H_2 productivity, the best performing sample at 500°C was 15-Ni/La-F. Stable activity was confirmed for at least 8 h-on-stream (Fig. 22). Non negligible selectivity to methane was a drawback, which may be limited by valorizing this byproduct as fuel to heat up the reformer, together with the spent reformate exiting from the fuel cell after operation. Indeed, typical 75% fuel utilisation is reported for PEM fuel cells [80], which usually suggests the installation of a post-combustor to improve the overall system efficiency.

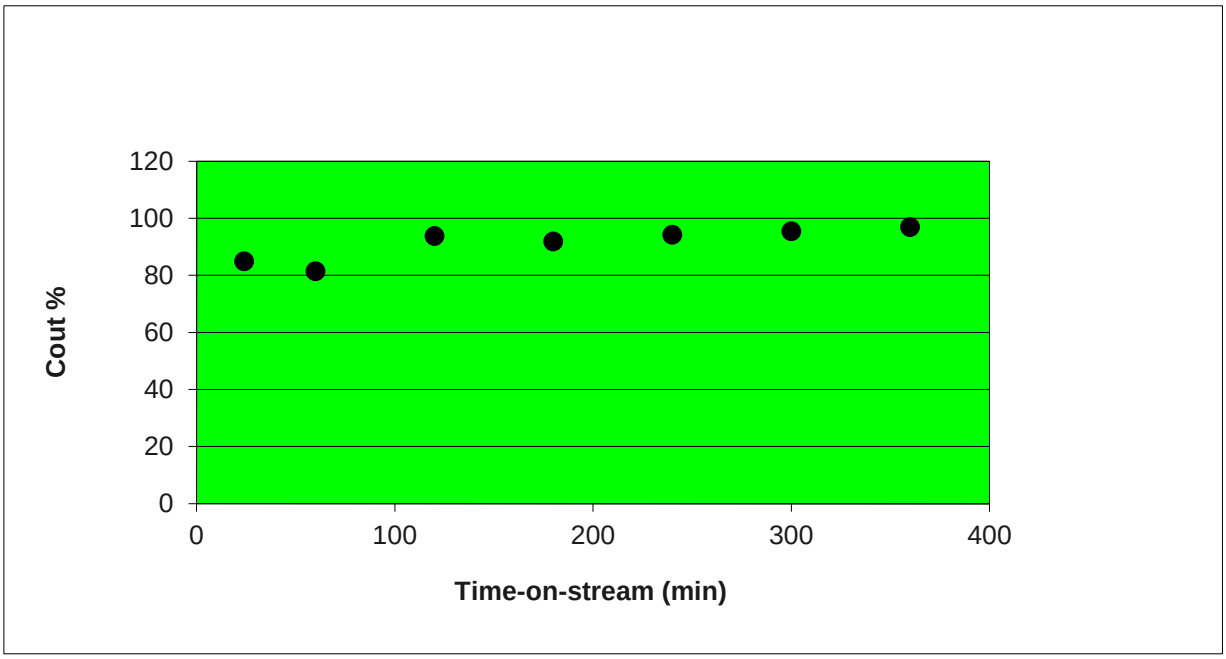

Fig. 22. Carbon balance 15-Ni/La-F catalyst.

3.6 Summary

Ni-based catalysts with different metal loading and supported over lanthana or titania were synthesized and tested for the steam reforming of ethanol. A new preparation procedure was proposed, *i.e.* flame pyrolysis, leading to high metal dispersion. This allowed to improve catalytic activity and most of all the resistance towards coking. Suitable thermal was also achieved during high temperature operation.

Satisfactory H_2 productivity was achieved at 750^{o}C, allowing to obtain a reformate flowrate sufficient to feed a 5 kW fuel cell by using 1.35 kg of the best performing

catalyst (conservative estimation without taking into account further H_2 production by WGS).

Attempts of process intensification were also done by decreasing the operating temperature to 500°C. Such a temperature is very critical as for coking. The FP procedure proved very effective to impart good dispersion, thus limiting the formation of C nanotubes. The intrinsic acidity of the support has also an important role to avoid ethanol dehydration to ethylene and its consequent polymerization to form additional coke. In this respect, lanthana was much more effective than titania. However, the support played also a key role on metal dispersion. The highest dispersion was achieved over lanthana, also thanks to the formation of mixed Ni-La oxides during the one pot FP synthesis.

3.7 Characterization of Ni/ZrO_2 catalysts

As was mentioned in the introduction part, one objective for this thesis was a strategy to better control the support acidity on Ni-based catalysts supported over zirconia by adding basic oxides such as CaO. Therefore, the effect of CaO-doping on the textural properties of the support was evaluated by means of N_2 physisorption. According to the IUPAC classification, ZNi [80] exhibits a IV-type isotherm containing a H3-type hysteresis, typical of materials that do not possess a well-defined mesoporous structure, with a surface area of approximately 140 m^2/g

(see Table 9). CaO-doping neither affected the structure nor the morphology of the support.

In order to identify the different NiO species on the surface area of the support and their reduction temperature, TPR measurements were carried out (Fig. 23).

Table 9 Specific Surface area by N_2 physisorption and crystal size (c.s.) as determined by O_2 chemisorption and Rietveld refinement for catalysts prepared by impregnation method.

	ZNi	ZCa_3Ni	ZCa_6Ni	ZCa_9Ni
Specific surface area (m^2/g)	141	150	142	135
c.s.$_{ZrO2}$ Rietveld (nm)	7.3	8.1	9.3	13.4
c.s.$_{Ni}$ Rietveld (nm)	3.2	2.8	3.4	4.5
D_{Ni} O_2Chemisorption (nm)	4.5	3.8	4.6	5.4

ZNi showed several reduction peaks, in a broad region between 250 and 550°C. Since it is known that Ni^{2+} is reduced to NiO without any intermediate oxide [82], the presence of several peaks suggests the existence of NiO species differently interacting with the support [52, 83]. The first peak can be assigned to non-interacting NiO, since unsupported NiO reduces at 280°C [84, 85], then is more easily reducible. The peak at about 380°C can be ascribed to NiO weakly interacting with the support, while the higher temperature peaks (between 480 and 520°C) indicates NiO species interacting stronger and stronger with zirconia [85, 86]. It seems that CaO doping increases the NiO fraction reducible at lower temperature as shown by the TPR profiles of the doped samples. A progressive

increase of the intensity of the first reduction peak, roughly proportional to the rise in CaO content, was observed. A decrease of metal dispersion is usually correlated to a decreaseof reduction temperature, as previously discussed and as reported in the literature [44, 45], which would negatively affect resistance to coking. Indeed,as previously reminded, smaller Ni particles are less prone to form carbon filaments. However, by looking at the crystal size variation reported in Table 9, just a small increase of Ni particles size can be observed with increasing CaO content.

Also the literature reports [83, 88] that an increased Ni reducibility in doped samples can be attributed to the formation of oxygen vacancies, which lead to easier NiO reduction by weakening the Ni-O bond. These oxygen vacancies, arise from the replacement of the Zr^{4+} cation with one and a lower positive charge (*i.e*. Ca^{2+}).

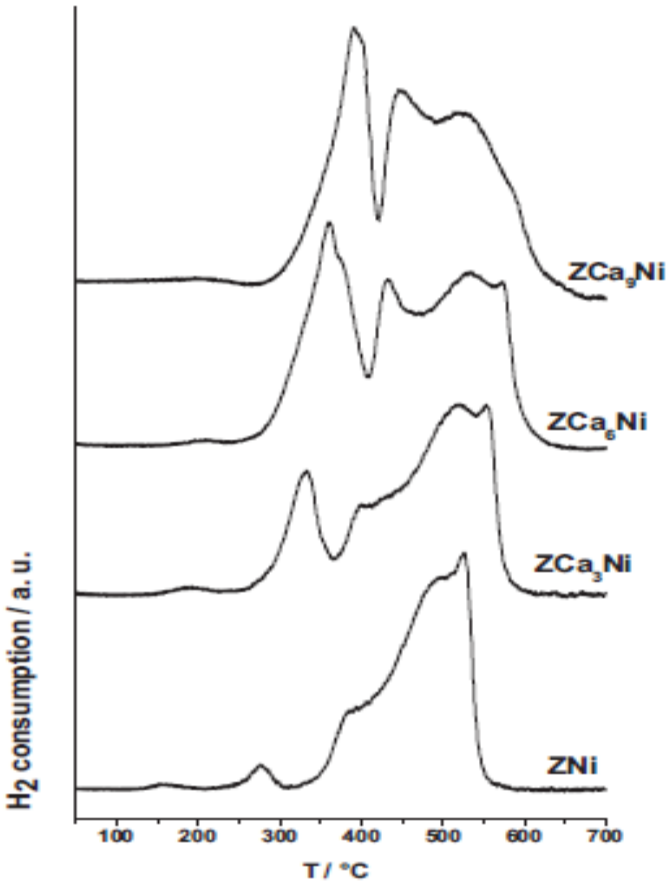

Fig. 23. TPR profiles of the catalysts with various CaO loading.

With the purpose to determine the zirconia structure and to ascertain if Ca^{2+} actually replaced Zr^{4+} in the lattice, XRD measurements were performed (Fig. 24) with Rietveld refinements. The spectra show that for zirconia support, the tetragonal phase is the only one present (*i.e*. the most intense peak at 2ɵ~ 30°), irrespectively of the CaO content.

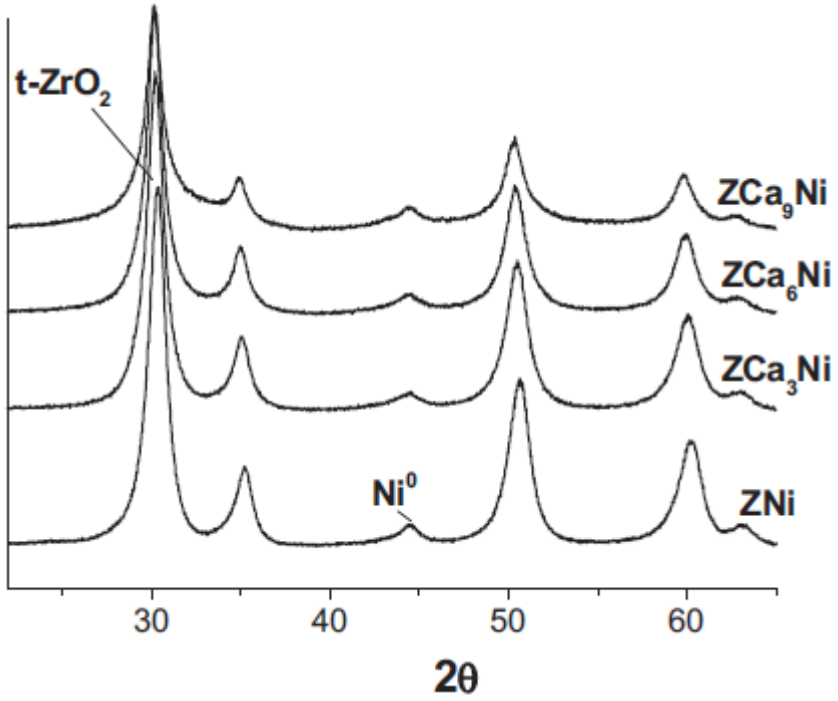

Fig. 24. XRD patterns of the reduced catalysts at increasing Ca content (from bottom to top).

Thus it may be concluded that CaO-doping did not affect the nature of ZrO_2 polymorph of the support. Nevertheless, a regular and incremental variation of the Rietveld-refined lattice parameters was observed as the CaO loading increased (Fig. 24). The increase of the cell volume can be taken as an evidence of Zr^{4+} (ionic radius 84 pm) substitution by Ca^{2+} (ionic radius 99pm) and supports the interpretation of the TPR results.

A regular and non-linear increase of crystal size of *t*-ZrO_2 (Table 9 and Fig. 25) was also noticed, while the fraction of crystalline zirconia decrease was observed as a function of increasing CaO content. The crystal growth was favored with the addition of CaO to the synthesis batch, which hinder the nucleation of *t*-ZrO_2.

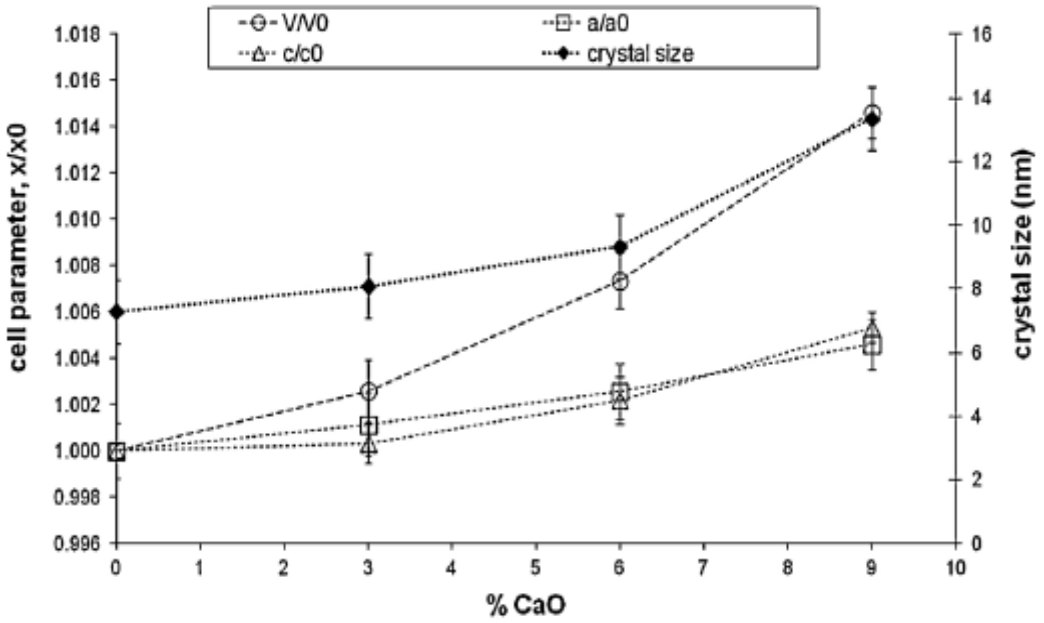

Fig. 25. Relative variation of the parameters (ratios of unit-cell constants, a/a_0, and c/c_0, and volume, V/V_0, where, a_0, c_0 and V_0 are the parameters of *t*-ZrO_2 without Ca) and crystal size of the zirconia phase as a function of the CaO loading.

The presence of metallic Ni (peak at 2ɵ = 44.5°) in all the samples, suggested that the reduction treatment at 500°C substantially reduced all Ni^{2+} to Ni^0.

A size estimate of Ni nanocrystals provided by Rietveld refinements of XRD patterns is reported in Table 10. The size of Ni crystallites slightly increased with increasing CaO content. These data are in perfect agreement with O_2 chemisorption (also in Table 9).FTIR was used to evaluate the surface acidity [88]. In Fig. 26, the admittance of 100 Torr CO onto the activated samples evidenced the formation of a unique spectral envelope either in the presence or in the absence of CaO: in particular, the band that formed in all cases was located in the spectral range 2170-2180 cm^{-1}.

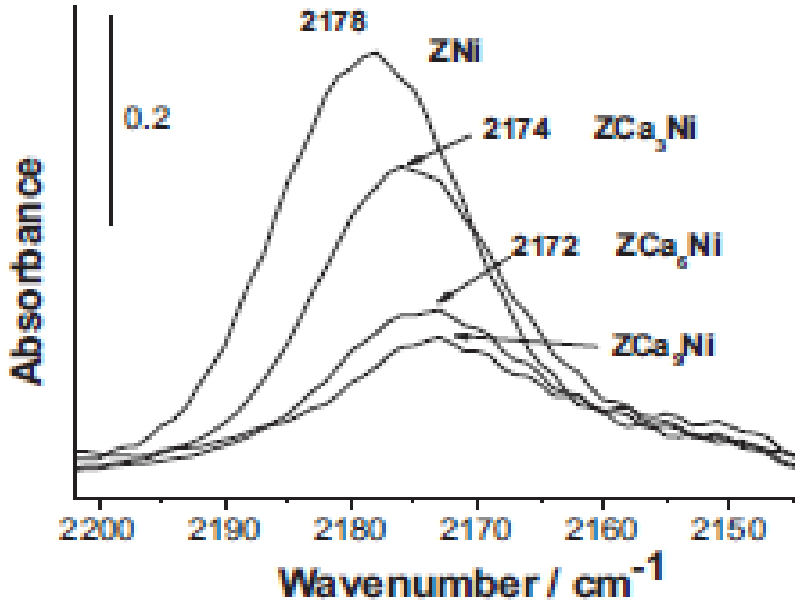

Fig. 26. FTIRspectra of adsorbed CO at RT on the reduced catalysts.

According to literature data [90], this band can be attributed to the ν_{CO} stretching mode of carbonyl-like species formed between CO and coordinatevely unsaturated Zr^{4+} cations located at the surface of all systems here under investigation (and set free by outgassing). Likewise, the addition of CaO provoked a decrease in the band intensity, which might indicate that CaO is likely to bring about a sort of external coating on top of the ZrO_2 species. Moreover, the shift of the CO band (from ~2178 to ~2172 cm^{-1}) indicates that the "shielding" effect induced by the CaO species was more efficient towards the high-ν component of the CO band envelope: this, in turn, means that the highly uncoordinated Zr^{4+} cations located in the most defective crystallographic positions (like high-index side terminations of the coin-like crystallites of ZrO_2) [91] are "shielded" by the dopant. Thus, the general acidity features of the catalysts are partially suppressed.

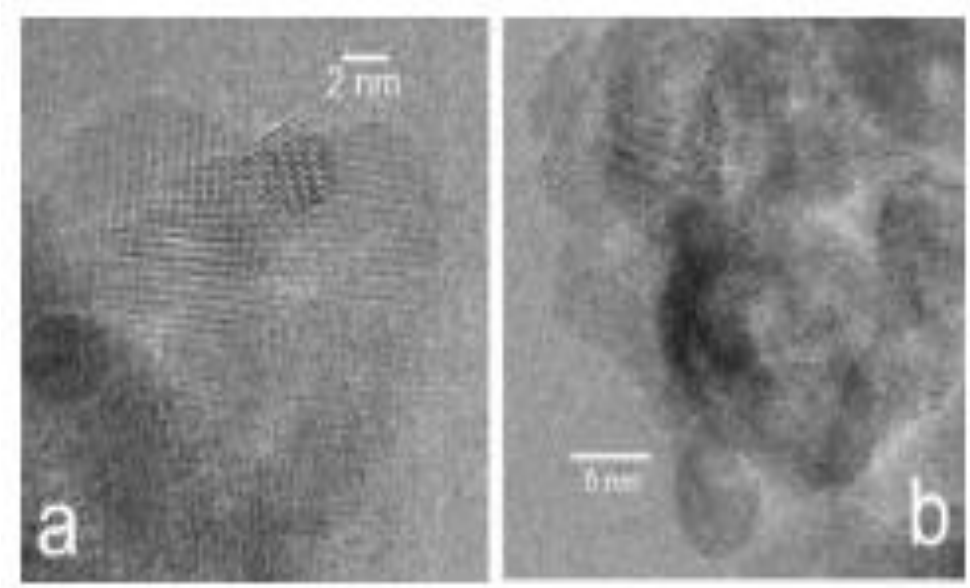

Fig. 27. TEM images of (a) ZNi; (b) ZCa_9Ni.

ZrO_2 particles with good crystallinity were observed in all the systems. They were highly ordered and highly packed each other as well, with average particle size 5-8 nm (In Fig. 27 a and b are reported both images). As it is observed in Fig. 27*b*, when the amount of CaO increased, a general lowering of the order was achieved, with the parallel evidence of an external partially amorphous habit. This amorphous over layer is rather thin and transparent, still permitting the observation of the particle's contours.

These characteristics are well consistent with the spectroscopic data reported in the previous section, as the decreasing intensity of the CO band is in good agreement with the partial amorphisation of the external habit of the catalysts due to the CaO dopant species. A decreased fraction of the crystalline zirconia phase, implying a larger content of the amorphous phase at high CaO loadings was also found by XRD.

Some conclusion could be that the specific surface area of the support did not change too much with the increased amount of CaO. Therefore, the Ni dispersion was similar. It means that all samples are made by small and dispersed Ni nanoparticles, which are essential in order to minimize coke formation.

On the contrary, the Lewis acidity of the support, also involved in coke deposition, was effectively reduced by the addition of CaO to zirconia, producing oxygen vacancies, which seem to affect Ni reducibility.

3.8 Activity Testing for Steam Reforming of Ethanol

Control of coke formation by adding basic oxides species

In previous work we tested the effect of base oxides NaO, MgO and CaO on Ni catalysts supported over zirconia prepared by precipitation and flame pyrolysis methods, the catalyst ZCaNi demonstrating, in both cases, superior catalytic activity (see Fig. 29).

Based on this results, we compared ZCaNi and ZNi catalysts prepared by precipitation and impregnation. The results for the activity testing at 500°C for these catalysts are reported in Tab 10. This temperature was sufficiently high to achieve interesting catalytic performance, but it was critical as for coking and possible catalyst deactivation as previously discussed. Therefore, it was selected for conservative comparison based on catalyst stability.

Tab. 10. Results of the SRE tests at 500°C, time-on-stream 8 h, data averaged out at 4-8 h-on-stream, GHSV= 2500 h^{-1}.

	Blank test	ZNi	ZCa_3Ni	ZCa_6Ni	ZCa_9Ni
EtOH conversion (%)	13 ± 5	100 ± 0	100 ± 0	100 ± 0	100 ± 0
C balance (%)	91 ± 2	88 ± 4	89 ± 4	89 ± 3	0.95 ± 3
H_2 productivity (mol/min kg_{cat})	—	0.96 ± 0.05	0.92 ± 0.11	0.96 ± 0.08	0.86 ± 0.05
CH_4 selectivity (%)	—	17.3 ± 0.4	3.4 ± 1.0	7.2 ± 1.2	13.1 ± 1.2

All the catalysts exhibited full ethanol conversion, with interesting H_2 productivity, though lower than the one achieved at higher reaction temperature [44]. As reported in Table 10, methane was the only by-product at this reaction temperature, without acetaldehyde nor ethylene. This selectivity to methane is expected at this relatively low temperature, since its formation is due to ethanol decomposition into CH_4 + CO + H_2, but its incomplete reforming is due to low reaction temperature. Selectivity to methane seems roughly correlated to Ni crystal size: the lowest the size, the lowest the CH_4 fraction still unreformed at 500°C, thus indicating higher activity towards SR of CH_4 at higher Ni dispersion. In addition, methane concentration was not correlated to possible catalyst deactivation, as is sometimes the case of ethylene and acetaldehyde; on the contrary, its concentration was roughly constant with time-on-stream.

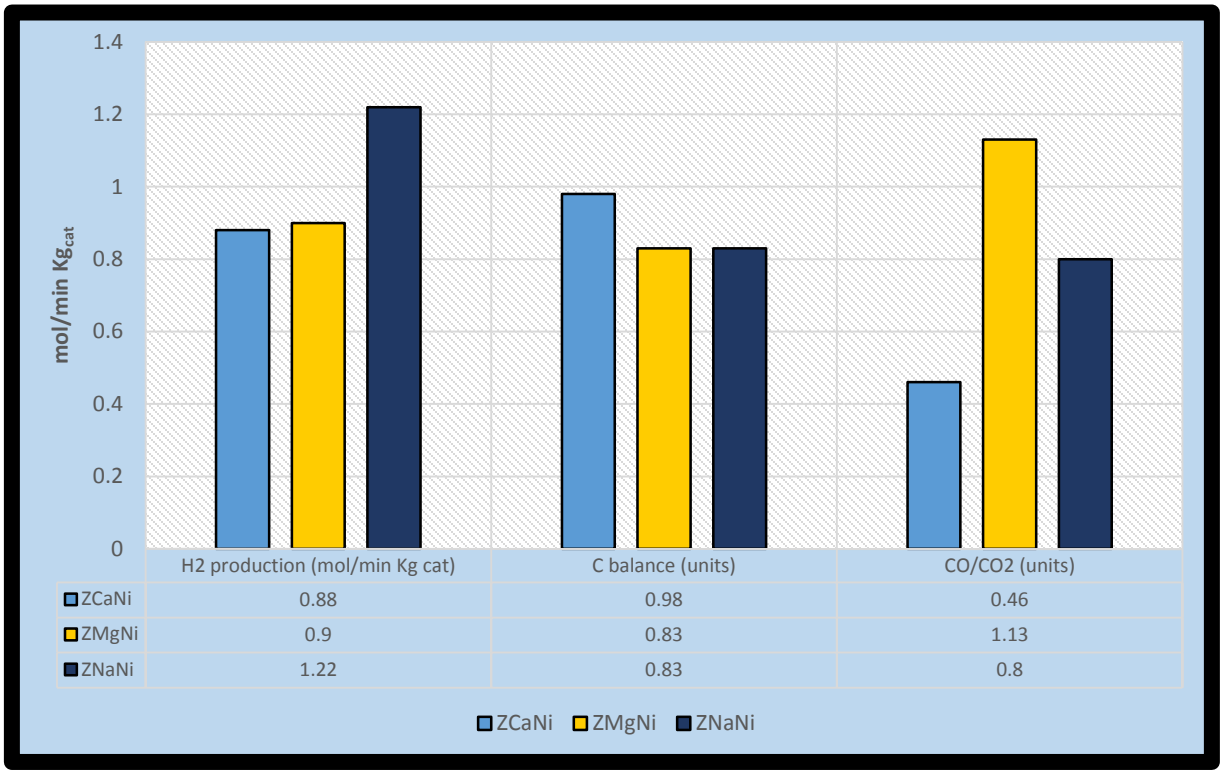

Fig. 28. Comparison on catalytic activity of steam reforming of ethanol at 500°C, GHSV= 2500 h^{-1} of base oxide-promoted Ni zirconia catalysts prepared by impregnation.

During the blank test, the C balance was 91%, with 13% ethanol conversion. This was attributed to some ethanol dehydration/decomposition over the quartz material filling the reactor. Another blank test was carried out with void reactor leading to almost nil ethanol conversion due to thermal decomposition at this temperature (<5%), but substantially full C balance. Limited coking activity was observed over Ni/ZrO_2 due to very high metal dispersion (confirmed for this samples series), which limits the accumulation of carbon filaments on the active phase with its consequent possible deactivation [44]. It is possible that the active phase remains active due to simple displacement from the support also in case of extensive filaments formation. In fact, due to accumulation of carbide species at the interface

between the metal and the support, filaments growth may provoke the detachment of the metal particle from the support surface. This may not induce to complete deactivation of the particle, since Ni remains exposed to the reactants and may still exploit its activity. However, some differences in selectivity may become evident, since the support play an important role in the activation of water, providing activated oxygen or oxydril species for the appropriate conversion of the reactants and intermediates to products. These oxidizing species cannot reach the CH_x species adsorbed on the metal because this is no more in contact with the support, provoking in this way the formation of by-products. However, the formation of carbon filaments is an important modification of the sample and may lead to possible reactor failure due to fouling and increasing pressure drop.

Poor metal dispersion is common correlated with the formation of carbon filaments, thus, smallest Ni particles may form less filaments. In this work, a substantially similar Ni dispersion should result in similar coking activity, or at least we would

expect a trend of C balance opposite to Ni crystal size. Whereas, C balance was found also correlated to CaO loading.

Indeed, the formation of some additional coke is expected due to ethylene polimerisation over acidic sites of the support. Thus, the modified acidity on this samples set may help limiting this additional coking feature.

Carbon balance increased to a small degree upon doping with CaO, reaching its maximum at the highest loading. For instance, in Fig. 29 (*a* and *b*) the carbon

balance significantly decreased within 8 h-on-stream for sample ZNi (*a*), whereas it was stable and high for ZCa_9Ni (*b*).

Based on negligible changes in H_2 productivity and ethanol conversion, it may be concluded that controlling the surface acidity by the addition of CaO may be beneficial to decrease the coking activity.

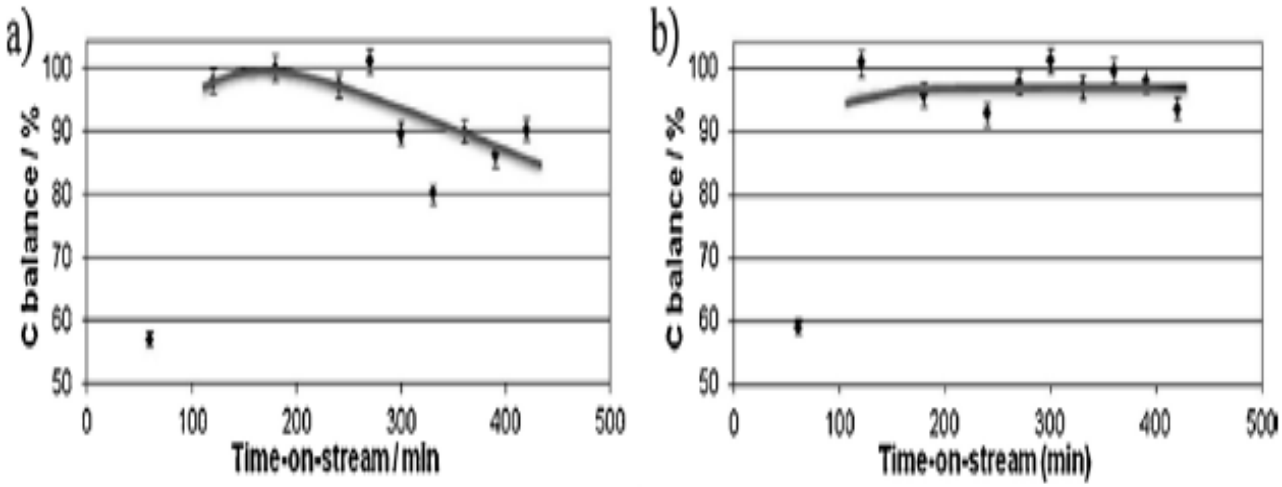

Fig. 29. Trend of C balance with time-on-stream for: (a) ZNi; (b) ZCa_9Ni.

By applying higher space velocity (7755 h^{-1}) more tests have been carried out for samples ZNi and ZCa_9Ni in order to underline the differences at lower conversion (Table 11). In general, the catalytic activity of sample ZNi was worse than the Ca-doped catalyst. Indeed, the steady state conversion was lower and the sample was mainly selective to acetaldehyde, whereas the activity of sample ZCa_9Ni was stable with time-on-stream and allowed to reach important H_2 productivity in spite

of the presence of unreformed by-products, whose selectivity remained as well constant for the whole duration of the test.

Table 11. Results of the activity test for ethanol steam reforming at 500°C, time-on-stream 8 h, data averaged out 4-8 h-on-stream, GHSV= 7755 h^{-1}.

	ZNi	ZCa_9Ni
EtOH conversión (%)	35 ± 7	53 ± 8
C balance (%)	93 ± 6	100 ± 4
H_2 productivity (mol/min kg_{cat})	n.d.	1.94 ± 0.10
Sel. CH_4 (%)	0	6.4 ± 1.0
Sel. CH_3CHO (%)	55 ± 11	35 ± 5
Sel. CH_2CH_2 (%)	0	4.9 ± 0.7

Another important feature on ZCa_9Ni is the presence of unreformed ethylene. Actually, its concentration remained stable for the whole duration of the test, indicating its incomplete reforming under these conditions, but at the same time insignificant coke formation by its polimerisation over the catalyst surface. By contrast, ZNi formed some unreformed ethylene (15% selectivity) during the first 2 h-on-stream, accompanied by higher ethanol conversion. Then ethylene disappeared from the reaction products, likely accumulating over the acidic sites of the support, and this was accompanied by a decrease of ethanol conversion, then stabilized to 35%. The difference of carbon balance was lower in this case.

As a promising catalyst based on resistance to coking, we carried out activity tests

at even lower temperature, at GHSV= 2500 h^{-1}, by using ZCa_9Ni (Table 12).

When the temperature was progressively lowered to 400°C and 300°C the ethanol conversion was unacceptably depressed. At 400°C the major byproduct was ethylene, its selectivity increasing with time-on-stream, though acetaldehyde also formed. The carbon balance became exceptionally low and decreasing with time-on-stream. This may suggest that coke accumulation occurred yet at 400°C over the active phase surface, which, in fact, decreased its activity with time-on-stream. Therefore, 500°C was considered the lowest temperature for safe operation with these catalysts.

A prolonged run was carried out at 500°C for 5 days (d1-d5) on the same ZCa_9Ni sample (Table 12). Catalyst performance remained stable for *ca.* 100 h-on-stream, without any decrease of ethanol conversion.

Table 12. Results of the activity test for ESR of sample ZCa_9Ni at different temperature and durability test at 500°C for 5 days. T-o-s: time-on-stream; d1-d5: days 1-5; GHSV = 2500 h^{-1}

	500°C	400°C	500°C_d1	500°C_d2	500°C_d3	500°C_d4	500°C_d5
EtOH conversion (%)	100 ± 0	82 ± 9 (dec. t-o-s)	100 ± 0	100 ± 0	100 ± 0	100 ± 0	100 ± 0
C balance (%)	95 ± 3	74 ± 11	91 ± 4	92 ± 6	91 ± 7	94 ± 2	89 ± 4
H_2 productivity (mol/min kg_{cat}	0.86 ± 0.05	0.3 ± 0.4	0.84 ± 0.05	0.85 ± 0.03	0.82 ± 0.06	0.84 ± 0.05	0.80 ± 0.03
Sel. CH_4 (%)	13 ± 1	2.1 ± 0.5	12 ± 2	14 ± 2	13 ± 4	13 ± 1	12 ± 2
Sel. CH_3CHO (%)	0	7 ± 2	0	0	1.1 ± 1.0	2.5 ± 0.4	1.7 ± 1.0
Sel. CH_2CH_2 (%)	0	20 ± 5 (inc. t-o-s)	0	0	0	0	0

Certain amount of acetaldehyde started forming after *ca.* 50 h-on-stream, on the contrary, ethylene was absent at reactor outlet.

When adding basic promoter, a beneficial improvement of catalyst resistance towards coking can be ascribed to the progressive decrease of the Lewis acidity of the support, which contributes to the side reactions leading to coke deposition. Moreover, CaO addition induced the formation of oxygen vacancies, which may activate CO_2 and H_2O, thus favoring the gasification of coke [83, 92, 93]. This is an important feature that, adding to good Ni dispersion and suppression of acidity allowed stable operation of the catalyst.

We also performed the characterization of the spent catalysts to better understand the coking phenomenon.

In Fig. 30 the Micro-Raman analysis showed the presence of both D and G bands of graphite that were attributed to the presence of multiwalled carbon nanotubes (MWCNTs) and to encapsulating coke due to polymerisation [94, 95]. In Fig. 31 the presence of some C (e.g. graphite layers) is evidenced over the surface of sample ZCa_9Ni. On the other hand, catalyst ZNi was predominantly characterized by the contribution of nanostructured carbon, represented in Figs. 32 as multiwalled carbon nanotubes (MWCNts), 33-37 nm in diameter, which were completely absent in sample ZCa_9Ni.

TPO was also carried out over the spent catalysts. Sample ZNi used for the standard activity testing (8 h-on-stream at 500°C) returned a carbon deposition rate

of 10.1 mg C/g_{cat} h-on-stream. When sample ZCa_9Ni was tested after the durability test (5 days-on-stream) a much more limited C accumulation was observed, corresponding to a rate of 0.75 mg C/g_{cat} h-on-stream. EDX analysis also qualitatively confirmed these data.

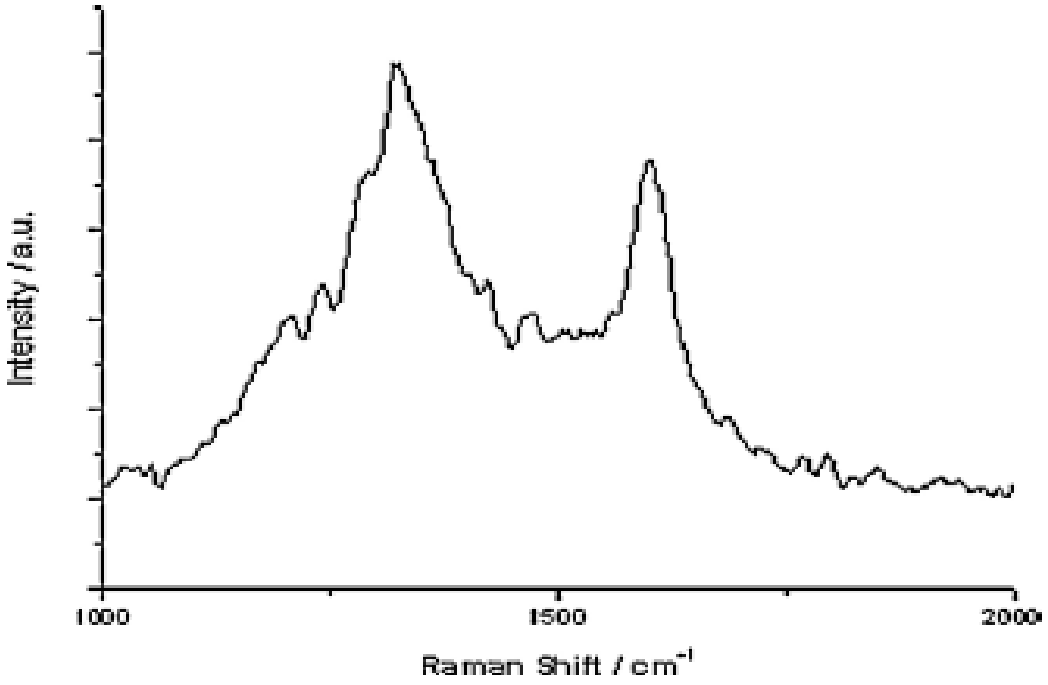

Fig. 30. Microraman spectra of the spent sample

Thus, the dehydration of ethanol to ethylene at low temperature is the responsible for some accumulation of coke. The titration of the strongest acidic sites with CaO may limit this phenomenon and additionally it can provide oxygen vacancies acting as activation sites for water and carbon dioxide, which helps cleaning the surface of the active phase.

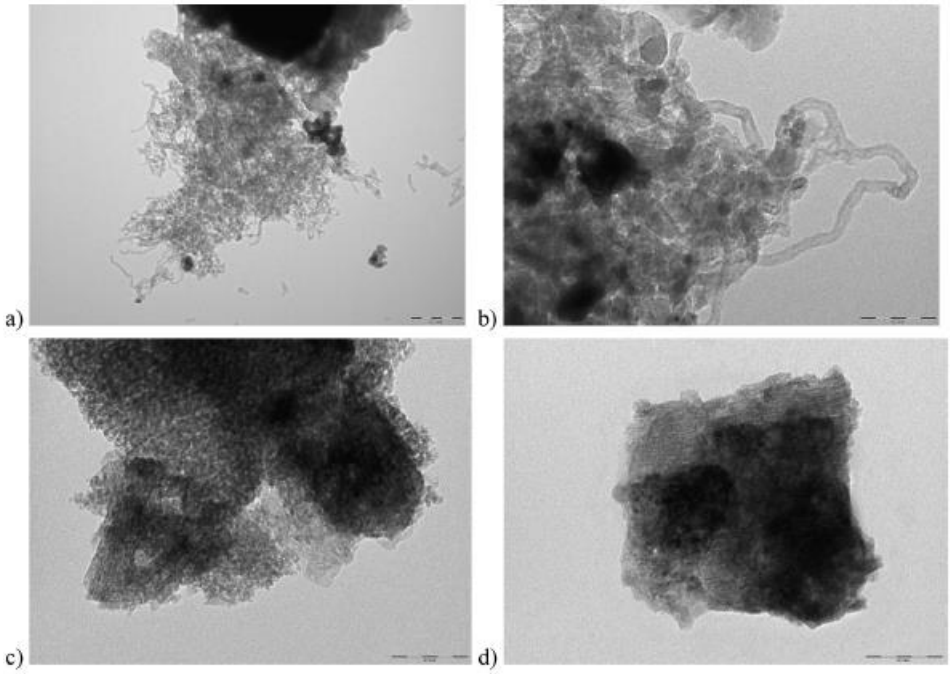

Fig. 31. TEM micrographs of spent samples ZNi sample. ZNi (a and b) and ZCa_9Ni (c and d).

In addition, Ni can induce the formation of MWCNTs, especially when poorly dispersed or not sufficiently stabilized by the support. As a result, in spite of the high Ni dispersion, similar for samples ZNi and ZCa_9Ni, CNTs were evident in the spent ZNi sample. For this reason, it can be also concluded that doping with CaO, and the consequent formation of oxygen vacancies, helps in cleaning up the surface by providing activated OH or O radicals, which are also able to stop the subsurface accumulation of carbon at the interface between Ni an the support. In this way the growth of CNTs is effectively inhibited.

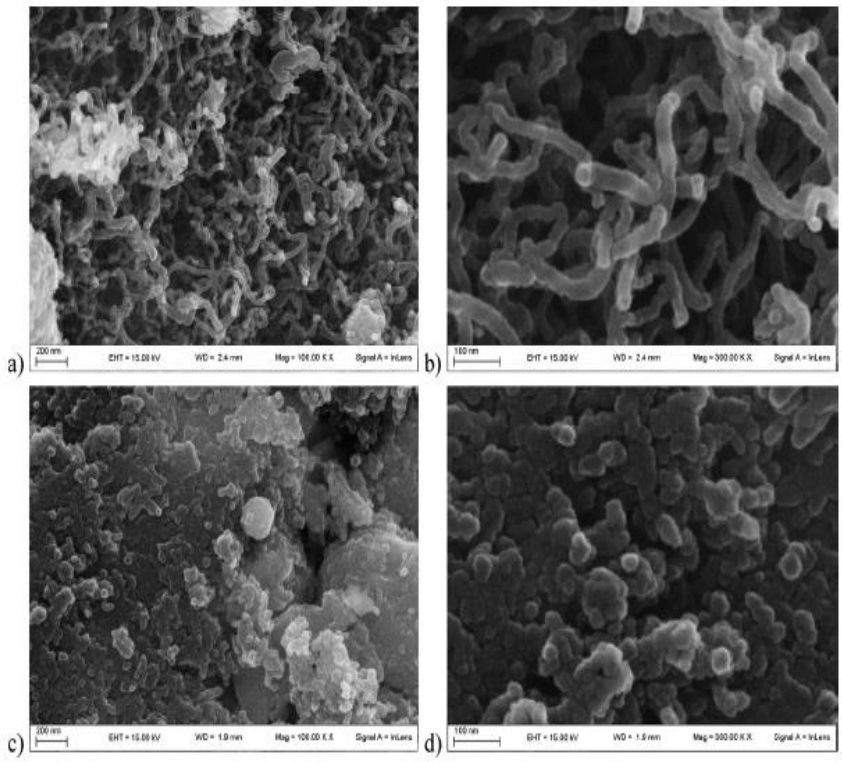

Fig. 32. FE-SEM images of spent samples ZNi (a and b) and ZCa_9Ni (c and d).

Effect of bioethanol concentration and purity

Base on the results mentioned above, in which ZCa_9Ni catalyst has demonstrated interesting catalyst performance, studies were carried out for process intensification and economic optimization by considering different ethanol concentrations. Therefore, two set of catalyst were used. The first one, Ni catalyst supported on zirconia prepared by flame pyrolysis. The second one, a group of Ni catalysts over zirconia prepared by flame pyrolysis with the direct incorporation of CaO during the synthesis. As solution for steam reforming reaction bioethanol was used at two concentrations, 90 (BE90) and 50 vol% (BE50), to be compared with

absolute ethanol (EtOH). Diluted bioethanol was produced through the PROESA process as second generation feedstock.

By comparing the tests at different temperatures (500, 400 and 300°C), independently of bioethanol concentration, the effect of CaO on NiZr was evidenced at 300°C where the catalyst doped with CaO demonstrated higher ethanol conversion comparing with those of the undoped catalyst (ZNi) (Fig. 33). While all the catalysts tested at 400 and 500°C regardless of the ethanol concentration resulted in full ethanol conversion. The highest H_2 productivity was reached at 500°C (Fig. 34) with both bioethanol concentrations due to the low selectivity to by-products at this temperature (Fig. 36).

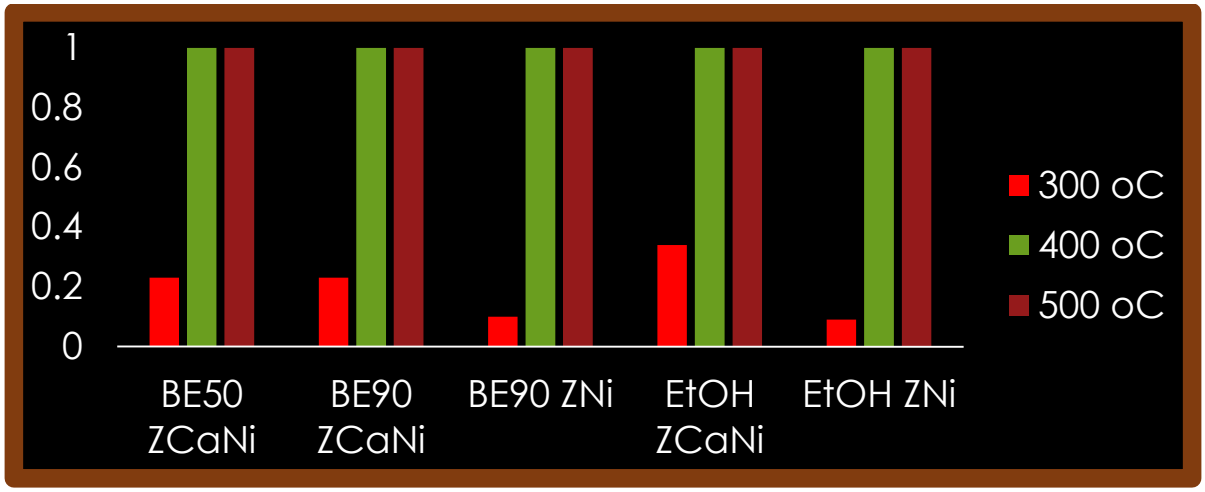

Fig. 33. Ethanol conversion of Ni/ZrO_2-F catalysts with and without CaO at different temperature.

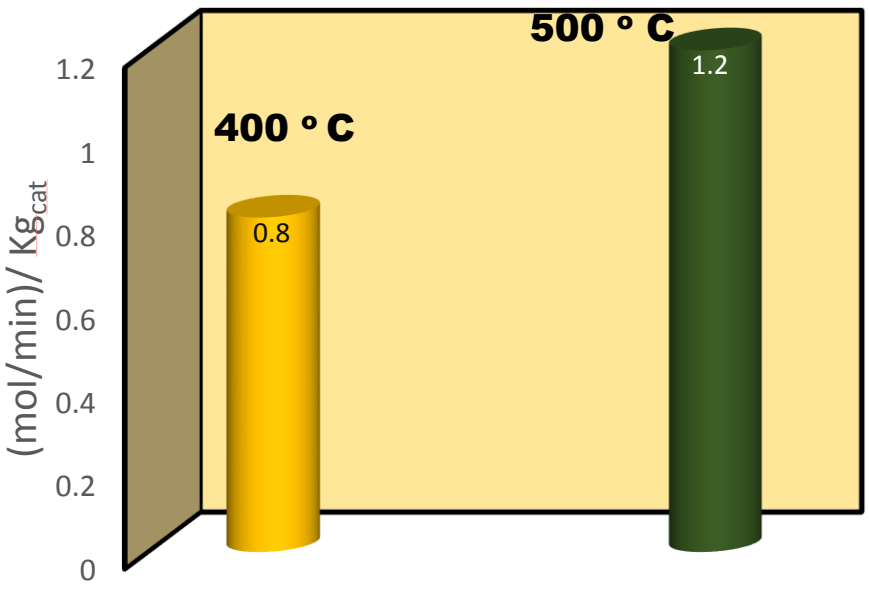

Fig. 34. Effect of Temperature reaction on H_2 productivity of 15-Ni/La-FP by using BE90

For instance, the acetaldehyde selectivity was almost zero at 400 and 500°C and at 300°C was higher especially for the catalyst without CaO (Fig. 36a). As for the carbon balance, the best results were exhibited by the ZCa_9Ni tested with BE90 and EtOH because at low temperature the limited acidity contribute to increase the carbon balance (Fig. 35). While carbon balance for ZCa_9Ni by using BE50 seem to be affected by possible impurities (such as sulphur and poisoning compounds in the BE solution) which obviously diminish catalyst activity. This was supported by TPO study that showed a lower presence of coke on this catalyst.

Although the results of H_2 productivity at the different temperatures tested are almost the same with both BE solutions, there are differences on C balance and selectivity to by-products, showing best results for BE90 (Fig. 35).

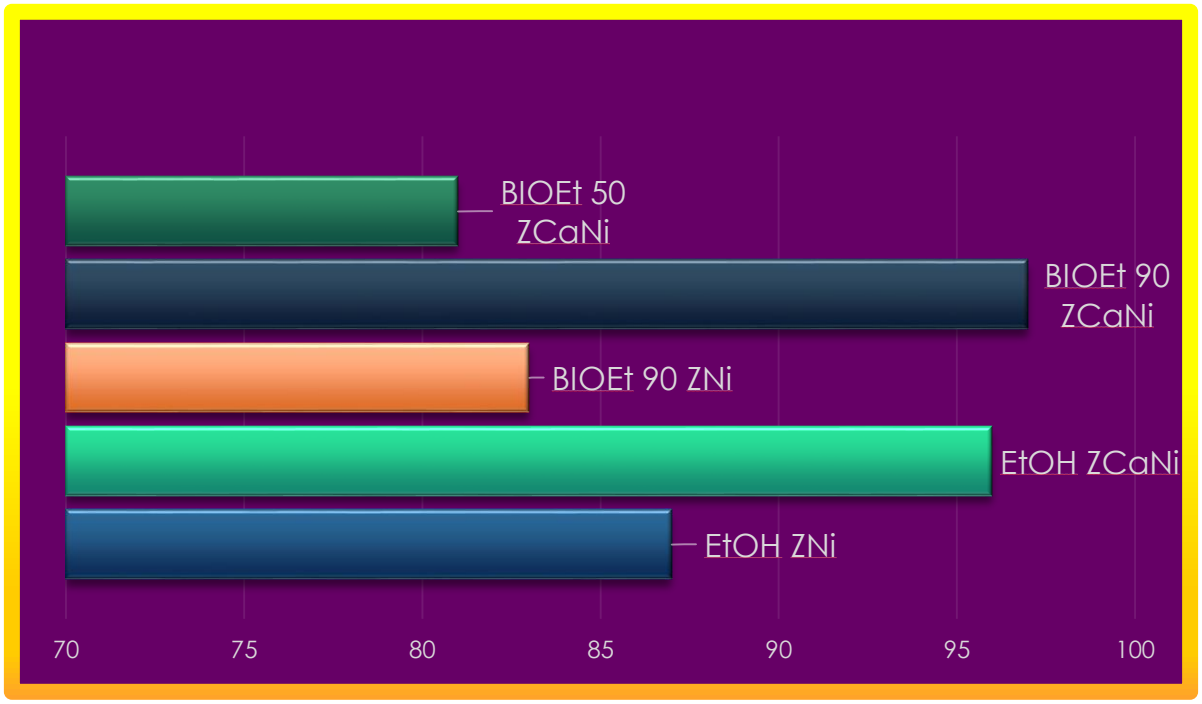

Fig. 35. Carbon balance (%) of Ni/ZrO_2 catalysts with different bioethanol concentrations.

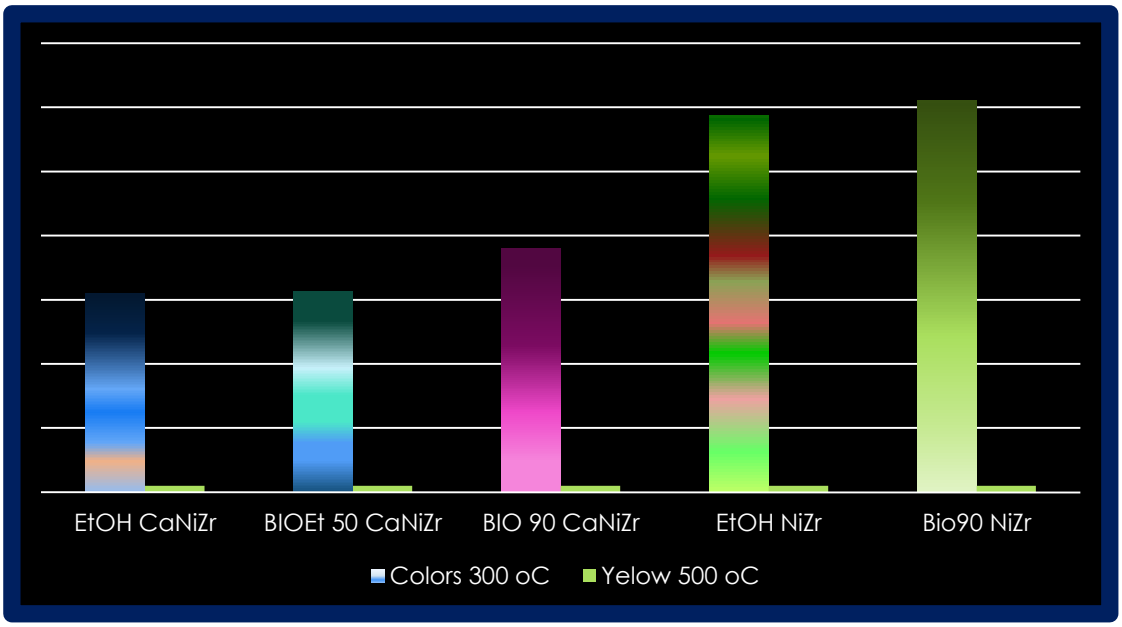

Fig. 36. a) Selectivity to acetaldehyde (%) at 300 and 500°C

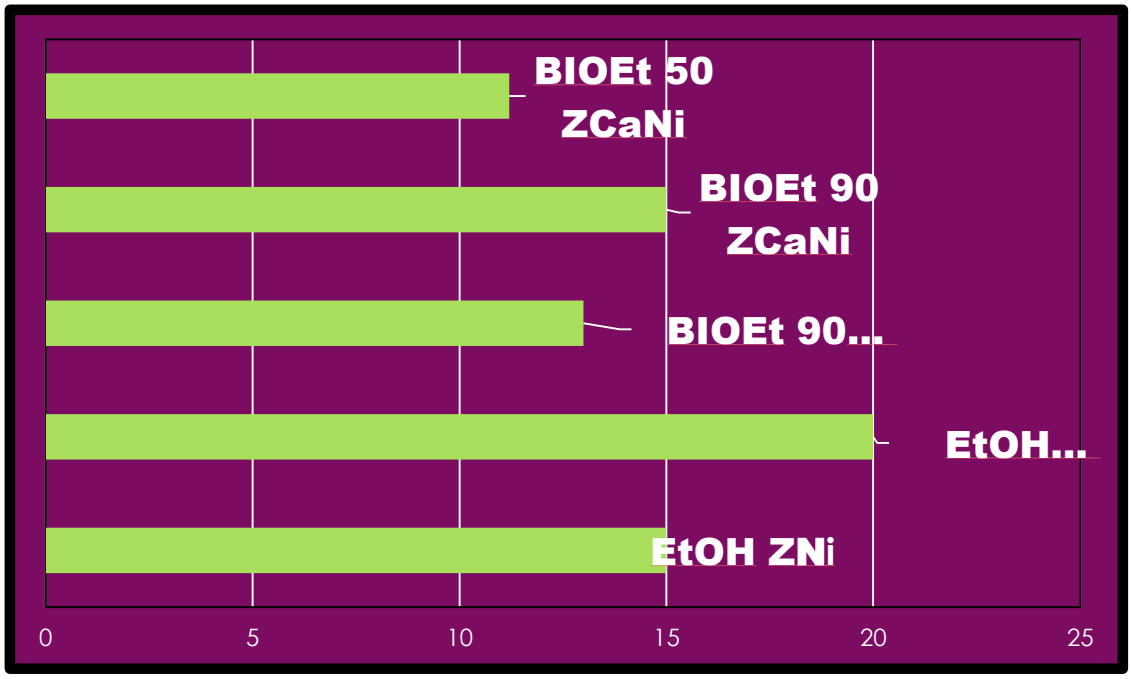

b) Selectivity to methane (stoichiometric units) at 500°C

3.9 Summary

Ni/ZrO_2 catalysts proved to be highly active for the ethanol steam reforming reaction. The presence of demonstrated coordinatively unsaturated Zr^{4+}, which contributes to Lewis acidity on the surface of the support, produces a little deactivation of the catalyst due to coke formation.

The addition of CaO to the support improved the resistance towards coking because of an effective control of Lewis acidity of Zirconia without affecting the nature of its polymorph structure.

Furthermore, the addition of CaO allowed the formation of oxygen vacancies, favoring the gasification of coke through the activation of CO_2 and H_2O. Also the formation of multiwalled carbon nanotubes was limited, because the Ni nanoparticles remind well dispersed in all the samples, important feature to keep low the coke formation.

CHAPTER 4
GENERAL CONCLUSION

The main purpose of this work involved catalytic processes to produce hydrogen from renewable sources, to be used as energy vector, *e.g.* for the cogeneration of electricity and heat through PEM fuel cells. Bioethanol was considered as feedstock for the renewable and sustainable production of hydrogen.

Results of our previous work have motivated to focus this project on promotion of a high metal dispersion, thus improving catalyst stability towards coking.

Effect of active metal loading and support dispersion.

For the performance of Ni-BEA catalyst formulation it was found that at 750°C productivity increased with Ni loading and increased activity for WGS reaction. At the lowest Ni loading unreformed ethylene and CH_4 were present, being completely reformed at highest Ni loading.

Additionally, comparing samples with the same Ni content (1.5%) but different Si/Al ratio, that means different acidity, full ethanol conversion was achieved with significant H_2 productivity and the C balance increasing with decreasing Al content (thus acidity). All the samples had more or less the same behavior, hence acidity

seems not to be determinant for the catalytic activity when operating at high temperature.

Also in the case of Ni based catalyst supported over Titania and Lanthana the catalytic activity improved with increasing the concentration of Ni. Also in this case, lower support acidity and higher Ni dispersion led to more stable and active catalyst.

Control of coke formation by adding of base oxide specie

Another strategy to control surface acidity was the addition of a basic promoter. The addition of 9 wt% CaO was effective from different points of view: i) directly decreasing surface acidity; ii) leading to good metal dispersion; iii) providing oxygen vacancies, able to activate water on the surface and thus cleaning it up.

Effect of Bioethanol concentration.

It is possible to use bioethanol 90 vol% for hydrogen production at 500^{o}C by using zirconia catalyst doped with calcium oxide which contribute to enhance the activity by better control of the support acidity.

Good catalytic performance can be obtained with ZCa_9Ni by using BE90 as well as with absolute ethanol working at 500^{o}C due to a better gasification of acetaldehyde byproduct at this reaction temperature.

BE50 can be used for steam reforming of ethanol with ZCa9Ni provided that there are not poison impurities on this bioethanol solution.

BIBLIOGRAPHY

[1] M. Ni, D.Y.C. Leung, M.K.H. Leung, Int. J. Hydrogen Energy, 32 (2007) 3238.

[2] A. Carrero, J.A. Calles, A.J. Vizcaíno, Appl. Catal. A: Gen 327 (2007) 82-94.

[3] A. Birot, F. Epron, C. Descorme, D. Duprez, Appl. Catal. B: Environ. 79 (2008) 17-25

[4] A. Benito, J.L. Sanz, R. Isabel, R. Padilla, R. Arjona, L. Daza, J. Power Sources 151 (2005) 11-17.

[5] A. Haryanto, S. Fernando, N. Murali, S. Adhikari, Energy Fuels 19 (2005) 2098-2106.

[6] INTA. http://bibing.us/proyectos/abreproy/3823/fichero/3.1+Producci%F3n+de +Hidr%F3geno.pdf

[7] P.Atkins, T. Overton, J. Rourke, M. Weller, F. Armstrong, M. Hageman, Shriver and Atkins. Inorganic Chemistry (Fifth edition). W.H. Freeman and Company, N.Y., 2010, pp383.

[8] "Introduction to Hydrogen and Hydrogen Communities", last modified July 20th 2005.

[9] http://www.eoearth.org/view/article/153620

[10] L. Canilha, A. K. Chandel, T. Suzane Dos Santos, F. A. Fernandes, W. L. Da

Costa, M. Das Graças Almeida and S. Silverio Da Silva. Journal of Biomedicine and Biotechnology 2012 (2012), 15 pages, doi:10.1155/989572.

[11] S. Ali, N. A. Mohd and D. Subbarao. Chem. Central Journal 5 (2011) 68.

[12] H. Balat, E. Kirtay, Int. J. of Hydrogen energy 35 (2010) 7416-7426.

[13] A. N. Fetsikostas, X.E. Verykios, J. Catal, 225 (2004) 439.

[14] H. Yoshida R. Yamaoka, M. Arci, J. Mol. Science, 16 (2015) 350-362.

[15] J. Llorca, N. Homs, J. Sales, P.R. de la Piscina, J. Catal. 222 (2004) 470

[16] F. Frusteri, S. Freni, V. Chiodo, L. Spadaro, O. Di Blasi, G. Bonura, S. Cavallaro, Appl. Catal. A: Gen 270 (2004) 1.

[17] B. Prakash, K. Deepak, Int. J. Hydrogen Energy, 32 (2007) 969.

[18] V. Nichele, M. Signoretto, F. Pinna, F. Menegazzo, I. Rossetti, G. Cruciani, G. Cerrato, A. Di Michele, Appl. Catal B: environ. 150-151 (2014) 12-20.

[19]http://www.topsoe.com/sites/default/files/topsoe_large_scale_hydrogen_ produc.pdf

[20] J. R. Rostrup-Nielsen and J. Sehested, Fuel Chem. Division Preprints, 48 (1) (2003) 218.

[21] M. Benito, J.L. Sanz, R. Isabel, R. Padilla, R. Arjona, L. Daza, J. Power Sources 151 (2005) 11-17.

[22] A.C. Furtado, C.G. Alonso, M. Pereira, N.R.C. Fernandez-Machado, Int.

J. Hydrogen Energy 34 (2009) 7189.

[23] D.L. Trimm, Catal. Today 37 (1997) 233-238.

[24] H. Song, L. Zhang, U. Ozkan. “Investigation of Bio-Ethanol Steam Reforming over Cobalt-based Catalyst” Conference. 2007 DOE Bio-Derived Liquids to Hydrogen Distributed Reforming Working Group (BILIWG) Meeting, November 6th , 2007.

[25] R.R. Davda, J.M. Shabaker, G. W. Huber, R.D. Cortright, J.A. Dumesic, Appl. Catal. B: Environ. 56 (2005) 171-186.

[26] A.N. Fatsikostas, D. Kondarides, X.E. Verykios, Catal. Today. 75 (2002) 145-155.

[27] D.K. Liguras, D.I. Kondarides, X.E. Verikios, Appl. B: Environ. 43 (2003) 345-354

[28] M. Benito, R. Padilla, A. Serrano-Lotina, L. Rodríguez, J.J. Brey, L. Daza, J. Power Sources. 192 (2009) 158-164.

[29] V. A. Kirillov, V.D. Meshcheryakov, V.A. Sobynin, V.D. Belyaev, Y.I. Amosov, N., A. Kuzin, et al. Theor. Found. Chem. Eng. 42 (2008) 1-11.

[30] J. Llorca, N. Homs, J. Sales, P.R. de la Piscina, J. Catal., 209 (2002) 306.

[31] D. K. Liguras, K. Goundani, X. E. Verykios, J. Power Sources, 130 (2004) 30.

[32] D. K. Liguras, K. Goundani, X.E. Verykios, Int. J. of Hydrogen Energy 29 (2004) 419-427.

[33] A. J. Vizcaíno, P. Arena, G. Baronetti, A. Carrasco, J. A. Calles, M. A. Laborde, N. Amadeo, Int. J. Hydrogen Energy, 33 (2008) 3489-3492.

[34] X. Hu, G. Lu, J. Mol. Catal. A: Chem. 206 (2007) 43-48.

[35] D. Wong, D. Montané, E. Chornet, Appl. Catal. A: Gen 143(1996) 245.

[36] R. R. Davda, J.W. Shabaker, G.W. Huber, R. D. Cortright, J. A. Dumesic, Appl. Catal. B: Environ. 43 (2003) 13-26.

[37] Z. Zhang, X. E. Verykios, Appl. Catal A: Gen. 138 (1996) 109-133

[38] G. Genti, S. Perathoner, Catal. TOday 148 (2009) 191-205.

[39] O. Christensen, D. Chen, R. Lødeng, A. Holmen, Appl. Catal. A. Gen. 314 (2006) 9-22.

[40] D. Chen, K.O. Christensen, E. Ochoa-Fernandez, Z. Yu, B. Tøtdal, N. Lattorre, A. Monzón, A. Holmen, J. Catal. 229 (2005) 82-96.

[41] A. Levant, F. Can, N. Bion, D. Duprez, F. Epron, Int. J. Hydrogen Energy 35 (2010) 5015-5020.

[42] A. J. Vizcaíno, A. Carrero, J. A. Calles, Int. J. Hydrogen Energy 32 (2007) 1450-1461.

[43] S. Cavallaro, N. Mondello, S. Freni, J. Power Sources 102 (2001) 198-204.

[44] I. Rossetti, C. Biffi, C. L. Bianchi, V. Nichele, M. Signoretto, F. Menegazzo,Appl. Catal. B: Environ. 117-118 (2012) 384-396.

[45] I. Rossetti, A. Gallo, V. Dal Santo, C. L. Bianchi, V. Nichele, M. Signoretto, ChemCatChem. 5 (2013) 294-306.

[46] I. Rossetti, J. Lasso, E. Finocchio, G. Ramis, V Nichele, M. Signoretto, Appl. Catal. A: Gen. 477 (2014) 42-53.

[47] A. Iriondo, V.L. Barrio, J.F. Cambra, P.L. Arias, M.B. Guemez, M.C. Sanchez-Sanchez, R.M. Navarro, J.L.G. Fierro, Int. J. Hydrogen Energy 35 (2010) 11622-11633.

[48] M. Lindo, A. J. Vizcaíno, J.A. Calles, A. Carrero, Int. J. Hydrogen Energy 35 (2010) 5895-5901.

[49] G. A. Deluga, J. R. Salge, L. D. Schmidt, X.E. Verykios, Science 303 (204) 993.

[50] S. Q. Chen, Y. Liu, Int. J. Hydrogen Energy 34 (2009) 4735.

[51] I.J. I. Coleman, W. Epling, R.R. Hudgings, E. Croiset, Catal. A. 363 (2009) 52.

[52] V. Nichele, M. Signoretto, F. Menegazzo, A.Gallo, V. Dal Santo, G. Cruciani, G. Cerrato, Appl. Catal. B: Environ. 111-112 (2012) 225-232.

[53] A. Le Valant, F. Can, N. Bion, D. Duprez, F. Epron, Int. J. Hydrogen Energy 35 (2010) 5015-5020.

[54] F. Zane, S. Melada, M. Signoretto, F. Pinna, Appl. Catal. A: Gen. 299 (2006) 137.

[55] G.L. Chiarello, I. Rossetti, P. Lopinto, G. Migliavacca, L. Forni, Catal. Today 117 (2006) 549-553.

[56] I. Rossetti, J. Lasso, V. Nichele, M. Signoretto, E. Finocchio, G. Ramis, A. Di Michele, Appl. Catal. B: Environ. 150-151 (2014) 257-267.

[57] S. Subramanian, Platinum Metal Rev. 36 (1992) 98.

[58] S. J. Tauster, S.C. Fung, R.I., Garten, J. Am, Chem. Soc. 100 (1978) 170.

[59] S. J. Tauster, A.cc. Chem. Res. 20 (1987) 389.

[60] H.M. Rietveld, J. Appl. Crystallogr. 2 (1969) 65 – 71.

[61] R.W Cheary. and A. Coelho, J. Appl. Crystallogr. 25 (1992) 109 – 121.

[62] I. Rossetti, J. Lasso, M. Compagnoni, G. De Guido, L. Pellegrini, Chem. Eng. Trans, 43 (2015) 229.

[63] G.L. Chiarello, I. Rossetti, L. Forni, P. Lopinto, G. Migliavacca App. Catal. B: Environ. 227–232.

[64] T.Tago, H. Konno, S. Ikeda, S. Yamazaki, W. Ninomiya, Y. Nakasaka, Catal. Today 164(2011) 158-162. Doi:10.1016/j.cattod.2011.10034

[65] E.L. First, C.E. Gounaris, J. Wei, C.a. Floudas, Phy. Chem 13 (2011) 17339.doi: 10.1039/c1cp 21731c.

[66] I.Rossetti, C. Biffi, L. Forni, Chem. Eng., 162 (2010) 768–775.

[67] I.Rossetti, O. Buchneva, C. Biffi, R. Rizza, App. Catal. B:

Environmental, 89 (2009) 383–390.

[68] J.M. Thomas, R.G. Bell and C. R. A. Catlow in Handbook of heterogeneous

Catalysis (Ed. G. Ertl, H. Knözinger and J. Weitkamp) (1977), Vol. 1, p. 206, VCH,

Weinheim.

[69] Atlas of Zeolite Framework Types. Fifth Revised Edition 2001. http://www.iza-structure.org/ZFT_low_res.pdf

[70] E. Finocchio, I. Rossetti, G. Ramis, Int. J. Hydrogen Energy. 38

(201) 3213–3225.

[71] V. Nichele, M. Signoretto, F. Menegazzo, I. Rossetti, G. Cruciani, Int.

J. Hydrogen Energy. 39 (2014) 4252–4258.

[72] V. Nichele, M. Signoretto, F. Pinna, E. Ghedini, M. Compagnoni, I.

Rossetti,Catal. Letters. 145 (2014) 549–558.

[73] J. Comas, F. Mariño, M. Laborde, N. Amadeo, Chem. Eng. J., 98, 1-2 (2004) 61-68.

[74] S. Thaicharoensutcharittanama, V. Meeyoob, B. Kitiyana, P. Rangsunvigita, T. Rirksomboona, Catal. Today, 164 (2011) 257-261.

[75] A. Ismail, D.W Bahnemann, J. Mater. Chem., 21 (2011) 11686-11707.

[76] A. Khataee, G.A. Mansoori, In nanostructured Titanium dioxide materials; World scientific, 2012.

[77] H. Muroyama, R. Nakase, T. Matsul, K. Eguchi, Int. J. Hydrogen Energy 35 (2010) 1575.

[78] Y. Liu, B. De Tymowski, F. Vigneron, I. Flores, O. Ersen, C. Meny, P. Nguyen, C. Pham, F. Luck, C. Pham-Hucc, ACS Catal., 3 (2013) 393-404.

[79] S.Y. Foo, C.K. Cheng, T. Nguyen, A. A. Adesina, Catal. Today, 164 (2011) 221-226.

[80] R. Koch, E. López, N. J. Divins, M. Allue, A. Jossen, J. Riera , J. Llorca. Int. J. of Hydrogen Energy 38 (2013) 5605-5615.

[81] IUPAC Recommendations, Pure Appl. Chem. 57 (1985) 603-619.

[82] Y.J.O. Asencios, E.M. Assaf, Fuel Process, Technol. 106 (2013) 247-252.

[83] J. D. A. Bellido, E. M. Assaf, J. Power Sources 177 (2008) 24-32.

[84] I., Zhang, J. Lin, Y. Chen, J. Chem. Soc., Faraday Trans. 88 (14) (1992) 2075-2078.

[85] Q.G. Yan, W.Z. Weng, H.I., Wan, H. Toghiani, R.K. Toghiani, C.U. Pittman Jr., Appl. Catal. A: Gen. 239 (2003) 43-58.

[86] Y.Q. Song, D.H. He. B.Q. Xu, Appl. Cat. A: Gen. 337 (2008) 19-28.

[87] V. García, J.J. Fernández, W. Ruíz, F. Mondragón, A. Moreno, Catal. Commun. 11 (2009) 240-246.

[88] J.D.A. Bellido, J.E. De Souza, J.C.M'Peko, E.M. Assaf, Appl. Catal. A: Gen. 358 (2009) 215-223.

[89] G. Herzberg, Molecular Spectra and Molecular Structure, II. Infrared and Raman Spectra of Polyatomic Molecules, Van Nostrand Co., New York, 1947, 274.

[90] G. Cerrato, S. Bordiga, S. Barbera, C. Morterra, Surf. Sci. 50 (1997) 377-379.

[91] C. Morterra, G. Cerrato, V. Bolis, S. Di Ciero, M. Signoretto, J. Chem. Soc. Faraday Trans. 93 (6) (1997) 1179-1184.

[92] Y.J. O. Asencios, J.D.A. Bellido, E.M. Assaf, Appl. Catal. A: Gen, 397 (2011) 138-144.

[93] T. Horiuchi, K. Sakuma, T. Fukui, Y. Kubo, T. Osaki, T. Mori, Appl.Catal. A: Gen. 144 (1996) 111-120.

[94] C. Gao, Y.Z. Jin, H. Kong, R.I.D. Whitby, S.F.A. Acquah, G. Y. Chen, H. Qian, A. Hartschuh, S.R.P. Silva, S. Henley, P. Fearon, H.W. Kroto, D.R.M. Walton, J. Phys. Chem. B 109 (2005) 11925.

[95] P. Delhaes, M. Couzi, M. Trinquecoste, J. Dentzer, H. Hamidou, C. Vix-Guterl. Carbon 44 (2006) 3005.